DEVELOPMENTAL NEUROSCIENCE

Structural insights into the formation of repulsive netrin guidance complexes

Jessica M. Priest[1,2,3], Ev L. Nichols[4,5], Robert G. Smock[6]†, Jesse B. Hopkins[7,8], Juan L. Mendoza[1,9], Rob Meijers[6,10], Kang Shen[4,5], Engin Özkan[1,2,3]*

Netrins dictate attractive and repulsive responses during axon growth and cell migration, where the presence of the receptor Uncoordinated-5 (UNC-5) on target cells results in repulsion. Here, we showed that UNC-5 is a heparin-binding protein, determined its structure bound to a heparin fragment, and could modulate UNC-5–heparin affinity using a directed evolution platform or structure-based rational design. We demonstrated that UNC-5 and UNC-6/netrin form a large, stable, and rigid complex in the presence of heparin, and heparin and UNC-5 exclude the attractive UNC-40/DCC receptor from binding to UNC-6/netrin to a large extent. *Caenorhabditis elegans* with a heparin-binding–deficient UNC-5 fail to establish proper gonad morphology due to abrogated cell migration, which relies on repulsive UNC-5 signaling in response to UNC-6. Combining UNC-5 mutations targeting heparin and UNC-6/netrin contacts results in complete cell migration and axon guidance defects. Our findings establish repulsive netrin responses to be mediated through a glycosaminoglycan-regulated macromolecular complex.

INTRODUCTION

Synaptic connectivity of the nervous systems in bilaterian animals is established through a conserved set of wiring molecules, including those that guide the growth of axons and determine synaptic partners (*1*–*3*). Netrins are conserved, secreted guidance cues that are unique in their ability to exert attractive and repulsive responses on growing axons (*4*). In addition to their neuronal functions, netrins and their receptors are known to control cell proliferation, migration, differentiation, and survival, and thus, they are targets for treating cancer and insulin resistance (*5*–*7*).

Netrins, known as UNC-6 in nematodes, act through two classes of receptors: Deleted in colorectal cancer (DCC)/neogenin class of receptors (named UNC-40 in nematodes) are required for both attractive and repulsive responses, while UNC-5 receptors are required only for repulsive responses (*8*). For attractive signaling, netrins can cause oligomerization or clustering of DCC or neogenin through the interaction of the receptors with multiple sites on netrin molecules (*9*, *10*). Such oligomerization likely leads to the proximity of intracellular signaling molecules recruited at motifs conserved in DCC/neogenin cytoplasmic domains (*11*). It is not clear, however, how netrin can induce repulsive responses, as there is only limited biochemical characterization and structural information for the proposed netrin–UNC-5 complexes.

Another important player in the netrin guidance system is glycosaminoglycans (GAG) such as heparan sulfate (HS), which are present on cell surfaces and in the extracellular matrix in the form of proteoglycans. Netrins were first purified from tissue with the help of their strong affinity for heparin (*12*). Their relevance for signaling has also been recognized, as lack of the HS-polymerizing enzyme, Ext1, leads to defective netrin- and DCC-mediated axon guidance in mouse spinal cord commissural neurons (*13*). Mutations in two HS proteoglycans (HSPGs), syndecan (SDN-1) and glypican (LON-2), show defects in UNC-6/netrin-mediated repulsive dorsal guidance of motor axons in *Caenorhabditis elegans*. A screen searching for mutations to enhance HSPG-dependent guidance pathway defects identified multiple *unc-5* mutants, hinting at an interaction between UNC-5 and HSPGs (*14*). Similarly, mutations in the HSPG *unc-52/perlecan* enhance distal tip cell migration defects of *unc-5* hypomorphs (*15*). An interaction between *C. elegans* UNC-40/DCC and the protein backbone of LON-2/glypican, proposed as a modulator of netrin-mediated axon guidance, has also been reported (*16*). Last, netrins can act as short-range or immobilized cues (*17*–*19*), where netrins would need to be immobilized within the growth substrate (*20*). Interactions with cell surface proteoglycans or the extracellular matrix can immobilize netrin and allow for signaling via mechanotransduction and haptotactic responses.

Given clear functional relevance and available structural models, HS binding has been proposed as a mechanism for regulating receptor selection and binding to netrins (*11*), although experimental evidence is lacking. It is not clear whether the contribution of GAGs is essential for signaling, as the major heparin-binding site of netrins, the C-terminal Netrin (NTR) domain (*21*), is not required for guidance activity of UNC-6/netrin (*22*) or binding to either DCC/neogenin or UNC-5 (*23*, *24*). As netrin without the NTR domain might still have some heparin-binding activity, it has been difficult to dissect the roles of GAGs in netrin signaling via simple domain deletions and truncations.

Last, the functional roles of HSPGs in axon guidance are not limited to netrin signaling. For example, HS is known to mediate interactions between other guidance cue-receptor pairs, including Slit and Robo (*25*), and the leukocyte common antigen-related protein (LAR) class of neuronal receptor tyrosine phosphatases to control neurite outgrowth (*26*, *27*). HS is also shown to interact with classical guidance cues Semaphorins and Ephrins (*28*).

[1]Department of Biochemistry and Molecular Biology, University of Chicago, Chicago, IL 60637, USA. [2]Institute for Neuroscience, University of Chicago, Chicago, IL 60637, USA. [3]Institute for Biophysical Dynamics, University of Chicago, Chicago, IL 60637, USA. [4]Howard Hughes Medical Institute, Stanford University, Stanford, CA 94305, USA. [5]Department of Biology, Stanford University, Stanford, CA 94305, USA. [6]European Molecular Biology Laboratory (EMBL), Hamburg Site, c/o DESY, 22603 Hamburg, Germany. [7]The Biophysics Collaborative Access Team (BioCAT), Argonne National Laboratory, Illinois Institute of Technology, Chicago, IL 60616, USA. [8]Department of Physics, Illinois Institute of Technology, Chicago, IL 60616, USA. [9]Pritzker School of Molecular Engineering, University of Chicago, Chicago, IL 60637, USA. [10]Institute for Protein Innovation (IPI), Boston, MA 02115, USA.
*Corresponding author. Email: eozkan@uchicago.edu
†Present address: AB Enzymes, Feldbergstrasse 78, 64293 Darmstadt, Germany.

While netrin's affinity for heparin-like molecules is well established, it is not clear whether the receptors interact with GAGs directly (*29*). Here, we chose to work with *C. elegans* UNC-6/netrin and UNC-5, the first molecules of their families to be identified, because they have clear axonal guidance and cell migration phenotypes and come with a large body of mutational and functional data. To study UNC-6–UNC-5 interactions and possible roles for heparin in this interaction, we established a yeast display system for UNC-5 and show that the binding between UNC-5 and UNC-6 is strongly enhanced when heparin is added. Through directed evolution of UNC-5 displayed on yeast, we have identified and engineered the UNC-5 interface used for heparin binding, and we confirmed heparin binding to this surface with a crystal structure of a complex formed between UNC-5 and a short form of heparin. The addition of heparin allows for the formation of the UNC-6–UNC-5 ectodomain complex with an unexpectedly rigid and globular structure, which mostly excludes the attractive receptor, UNC-40. We have shown that abolition of heparin affinity of UNC-5 in *C. elegans* results in cell migration defects associated with loss of function of *unc-5* and *unc-6*, indicating mechanistic dependence of netrin:UNC-5–mediated guidance on HS. Last, we show that the mammalian netrin-1–UNC5B complex is also strongly enhanced by HS, which competes with DCC binding to favor Unc5B binding, demonstrating conservation between the nematode and mammalian systems. Our results provide detailed biochemical and functional insights into repulsive netrin complexes and may be crucial in explaining chemo- and haptotactic responses to netrin sources.

RESULTS

High-affinity UNC-6–UNC-5 binding depends on heparin

The interactions of UNC-6/netrins with their attractive receptors, DCC and neogenin, have been heavily characterized using structural and mutational studies (*9*, *10*). However, structural data for netrin interactions with its repulsive receptor, UNC-5, remain sparse, likely due to the low affinity for this ligand-receptor pair. To study UNC-6/netrin–UNC-5 interactions, we established a yeast surface display system as a platform to measure and engineer this interaction, which also enabled us to investigate the effects of additional molecular players, most importantly, GAGs. Briefly, we displayed on yeast cells the ectodomain of *C. elegans* UNC-5, including its two immunoglobulin (IG) and two thrombospondin type I (Tsp1) domains, by way of a fusion to the yeast cell wall protein, Aga2 (Fig. 1A). UNC-5 is expressed on yeast cells as evident from antibody staining of the C-terminal myc tag. To measure UNC-6/netrin binding to UNC-5–expressing cells, we expressed and purified a soluble construct of *C. elegans* UNC-6 lacking its C-terminal NTR domain (UNC-6ΔC), because the NTR domain is known to limit solubility (*23*) and is dispensable for much of its function. We created a yeast-staining reagent by biotinylating UNC-6ΔC (fig. S1A) and incubating it with Alexa Fluor 647–coupled streptavidin. In the absence of heparin, UNC-6ΔC binds very weakly to UNC-5–displaying yeast, as measured with flow cytometry by the weak fluorescence shift relative to the negative control yeast (Fig. 1B, red). To test whether the interaction can be improved by GAGs, we added heparin (from porcine intestinal mucosa, ~16 kDa) and UNC-6ΔC on UNC-5–expressing yeast, which showed strong UNC-6 binding (right shift of the fluorescence histogram) with an apparent dissociation constant (K_d) of 35 nM in the presence of 0.31 μM heparin (5 μg/ml) [Fig. 1, A (right) and B (green), and fig. S1C]. This demonstrates that strong UNC-6–UNC-5 binding may require heparin, likely in the form of an HS proteoglycan on the growth cone or the substrate tissue in vivo.

Heparin dependence of UNC-6–UNC-5 binding can be modulated with directed evolution

We hypothesized that we can modulate UNC-5 dependence on heparin for UNC-6 binding using directed evolution. We created an UNC-5 ectodomain display library using random error-prone polymerase chain reaction (PCR) and selected for UNC-6ΔC binding while decreasing heparin concentrations in the staining solution (Fig. 1C). The third and final round of selections was performed in the absence of added heparin and therefore shows a slight reduction in binding compared to the previous round. We were able to evolve high-affinity UNC-6 binding as seen in titrations on yeast (Fig. 1D and fig. S1C). Sequencing of eight clones from the third round of selection shows that every clone included either an N18K or an N188K mutation (Fig. 1D). As these mutations increase net positive charge on UNC-5, we predicted that we had increased UNC-5 affinity to heparin, in addition to strengthening binding to UNC-6. Because we could observe strong UNC-6 binding with these mutants even in the absence of added heparin, binding might be supported by an endogenous, unknown GAG-like molecule on the yeast surface. Alternatively, purified UNC-6 used for selections might carry over an undetected GAG or GAG-like molecule as insect cells used for protein expression are known to make GAGs. Last, it is possible that the N➔K mutations might have also led to some increase in UNC-5–UNC-6 affinity independent of heparin.

To confirm that the two mutations identified are the cause for increased UNC-6ΔC binding in yeast display experiments, we performed titrations of UNC-6ΔC binding to UNC-5 N18K/N188K ectodomain on yeast in the absence of added heparin (Fig. 1E). Apparent binding affinities of UNC-6ΔC to UNC-5 N18K and N188K-expressing yeast were relatively strong and in the nanomolar range, 8.2 and 16.4 nM, respectively.

UNC-5 binds heparin via a positively charged patch at the boundary of its IG1 and IG2 domains

To gain more insights into UNC-5 interactions with heparin and/or UNC-6, we set out to determine the structure of the *C. elegans* UNC-5 ectodomain. Crystallization was successful for a construct containing the two IG domains, which included both N18 (IG1) and N188 (IG2) identified in directed evolution experiments. Using these crystals, we determined the structure of the two-IG domain UNC-5 construct to 2.9 Å resolution (Fig. 2A). The structures of the immunoglobulin domains show no major differences to previously determined human Unc5A, rat Unc5D (*30*, *31*), and mouse Unc5B crystal structures (*32*), including a buried disulfide bond linking UNC-5 Cys^{37} (C strand) and Cys^{84} (F strand) in IG1 in addition to the canonical disulfide bond found in IG domains, and a short α helix connecting E and F strands in IG1. Similarly, the IG2 domain is N-glycosylated at a remarkably conserved site, Asn^{178} (F strand), also observed in the rat Unc5D and mouse Unc5B structures; no glycosylation on IG1 is observed. We also had the opportunity to compare flexibility at the IG1-IG2 boundary: An alignment of our UNC-5 IG1 + 2 structure with three vertebrate UNC5 structures show wide variability of the angle between the IG1 and IG2 domains (fig. S2A). Flexibility at this position may be necessary for recognition by HS as well as protein ligands,

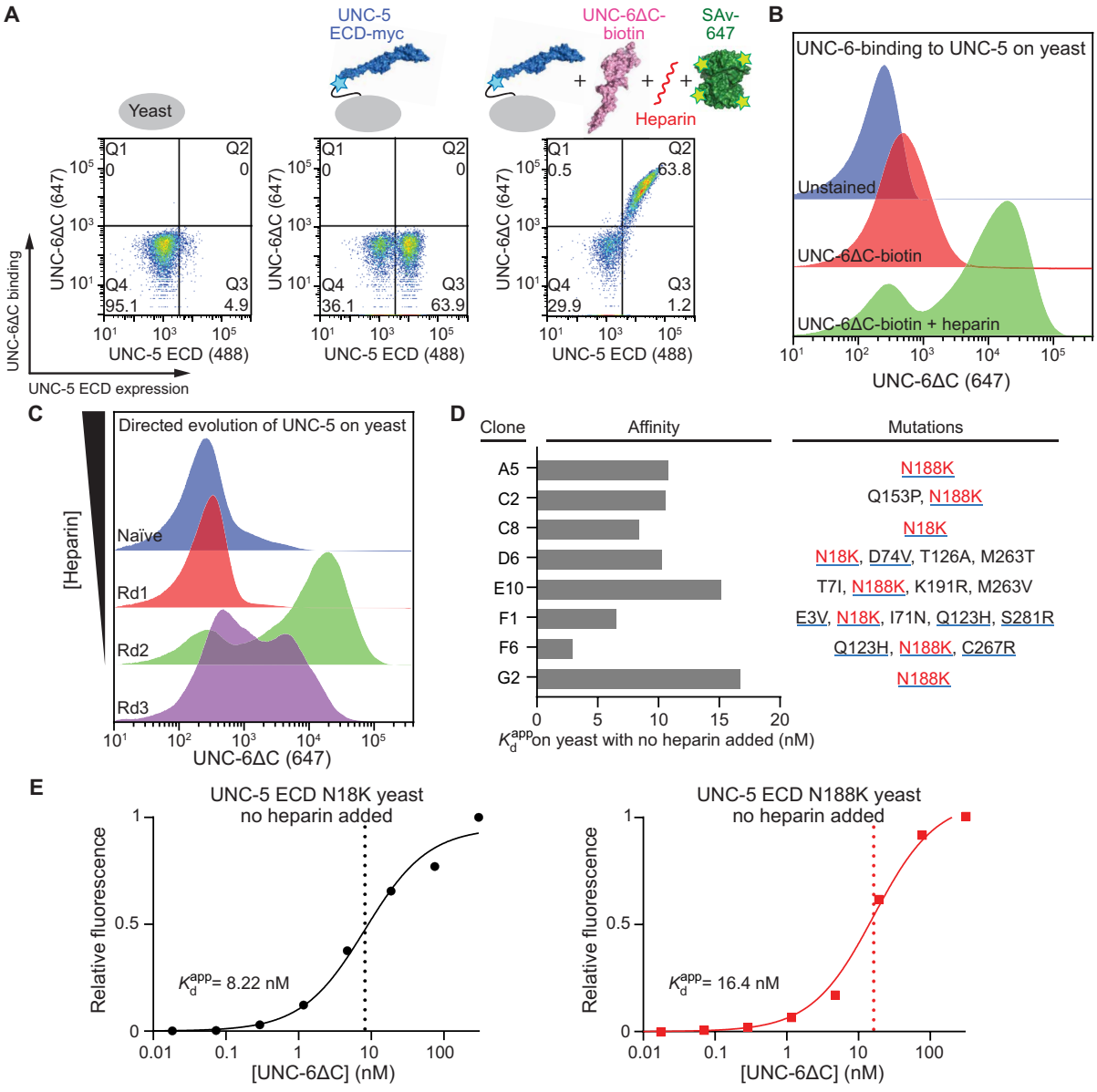

Fig. 1. UNC-5 affinity for UNC-6 is increased following directed evolution of UNC-5 ectodomain using yeast surface display. (**A**) UNC-5 ECD (extracellular domain) displays on yeast, as detected by anti-myc staining (Alexa Fluor 488), and strongly interacts with biotinylated UNC-6ΔC monomers bound to Alexa Fluor 647–coupled streptavidin in the presence of heparin. Left; Unstained cells. Middle: Cells stained with anti-myc antibody. Right: Cells double-stained with anti-myc and UNC-6ΔC–streptavidin with heparin (5 μg/ml) added. (**B**) Histograms for Alexa Fluor 647 fluorescence of unstained cells (blue), UNC-6ΔC–stained cells (red), and UNC-6ΔC-stained cells in the presence of heparin (5 μg/ml; green). (**C**) Histograms of bulk UNC-6ΔC labeling of the yeast library displaying randomly mutated UNC-5 ECD variants, including naïve library (blue), and resulting libraries during three rounds of selections, where heparin concentration was decreased. The final round of selection contained no added heparin. (**D**) Apparent UNC-6ΔC–binding affinities for the selected UNC-5 variants on yeast. All binding isotherms are shown in fig. S1C. Mutations increasing net positive charge on UNC-5 ECD are underlined blue; no mutation in the selected colonies added net negative charge. Data were collected in the absence of added heparin. (**E**) Binding isotherms repeated for two single-site mutants of UNC-5 ECD, N18K and N188K, interacting with UNC-6ΔC in the absence of added heparin.

because our directed evolution results indicate this region (containing Asn[18] and Asn[188]) as a site of HS binding, and this is also the binding site for Latrophilins (*31*).

There was unexplained electron density surrounding the IG1-IG2 boundary (figs. S2, B and C). On the basis of the presence of ammonium and lithium sulfate in the crystallization solution and the chemistry around the unexplained density, we believe that there may be two or more fully or partially occupied sulfate ions at this site. The surface electrostatic potential of our UNC-5 structure shows an intensely positive region at this domain boundary created by multiple arginines and lysines (Fig. 2B). Furthermore, the two N→K mutations selected in our directed evolution experiments fall in this region

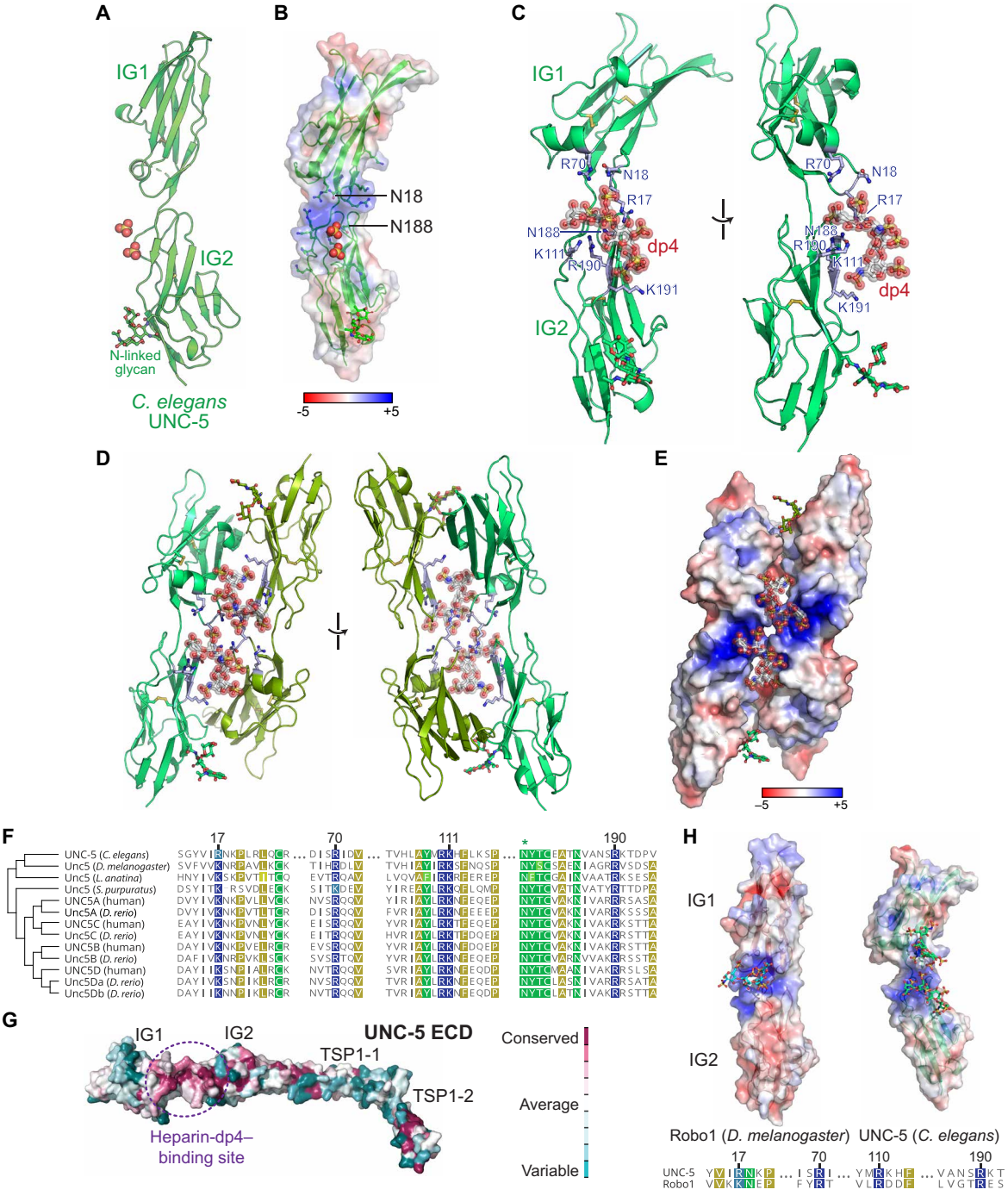

Fig. 2. Crystal structures of UNC-5 IG1-2 highlight a positively charged surface used for HS binding. (**A**) UNC-5 IG1-2 structure with putative sulfates bound near the IG1-IG2 boundary. The conserved N-linked glycan at N178 is shown in ball-and-stick representation. (**B**) Electrostatic potential surface for the UNC-5 IG1-2 structure, showing a positively charged surface at the IG1-IG2 boundary. The range of electrostatic potential used to color the surface is from −5 to +5 *kT/e*. The two Asn residues identified in directed evolution experiments are labeled. (**C**) Crystal structure of the UNC-5 IG1-2 domains bound to the heparin tetrasaccharide (dp4); one alternate conformation is displayed. For details, see fig. S2 (E to F). (**D**) The asymmetric unit of the UNC-5 + dp4 crystal structure, showing a possible dimer created by a dp4 molecule, built as two alternate conformations into density (fig. S2, B to D). The two alternate conformations overlap with two alternates of a dp4 molecule from the neighboring asymmetric unit, creating a four-molecule UNC-5 entity as seen in fig. S2D. (**E**) Surface potential of the dimer shows a contiguous positive surface, which is used for binding to HS. (**F**) The positively charged patch at the UNC-5 IG1-IG2 boundary is conserved. Alignment of protostome and deuterostome UNC-5 sequences show that positive charge at the IG1-IG2 boundary is highly conserved. Sequence numbering above follows the *C. elegans* UNC-5 sequence. (**G**) Surface conservation analysis by ConSurf of the ectodomain of UNC-5 (using the AlphaFold2 model) shows the IG1-IG2 boundary as the largest conserved surface patch. (**H**) Top: Side-by-side views of the *C. elegans* UNC-5 IG1-2 + dp4 structure and fruit fly Robo1 IG1-2 + dp8 structure (PDB ID: 2VRA; only a tetrasaccharide is visible), with surface electrostatic potentials. Bottom: Sequence alignment of UNC-5 and Robo1 IG1-IG2 domain contacts, showing that the positively charged patch at the IG1-IG2 boundary is common to both receptors.

interspersed between the positively charged arginines and lysines. Overall, this site is a strong candidate for HS binding.

We next crystallized and determined the structure of UNC-5 IG1 + 2 domains in the presence of a short heparin oligomer limited to four saccharide units, dp4, in a different crystal form. We observed strong extra density resembling an oligosaccharide oligomer in the same region, surrounded by Arg^{17}, Arg^{70}, and Arg^{190}; Lys^{111} and Lys^{191}; and Asn^{18} and Asn^{188} (Fig. 2C and fig. S2, E and F).

The UNC-5–heparin-dp4 crystals have an UNC-5 dimer in the asymmetric unit created by 1210 $Å^2$ of buried surface area, which appears to be held together partly by heparin interacting with both chains (Fig. 2D). While the extra density for heparin is strong, there is some ambiguity in the exact orientation of the dp4 ligand, including the glycan residue register and direction: As our best interpretation of density, we chose to model dp4 in two alternate conformations in equivalent positions within this dimer, which then overlap with their alternate conformations from the neighboring asymmetric unit's dp4 molecules (fig. S2, C, E, and F). An intimate tetramer, held together by and surrounding heparin molecules, is observed upon investigation of neighboring asymmetric units, where protein-protein contacts bury 1310 and 1120 $Å^2$ between UNC-5 chains related by crystallographic symmetry (fig. S2D). While these molecular interfaces may be physiological in the context of a heparin-mediated UNC-5 or UNC-6–UNC-5 oligomer, we do not yet have evidence to support such a model.

The IG–heparin interaction observed in the UNC-5–heparin complex may be a common feature of IG-superfamily receptors

Because of its sulfation and negative charge, heparin binding strongly favors positively charged surfaces on proteins. As a strongly positively charged protein, UNC-6 [isoelectric point (pI) = 8.7] binding to heparin is expected. However, UNC-5 ectodomain has a pI of 5.7, and a net predicted charge of −8 at pH 7. The heparin–UNC-5 interactions are a result of local charge at the IG1-IG2 boundary as observed in our crystal structure (Fig. 2E). The positively charged amino acids that create the HS-binding site in nematode UNC-5 are conserved across all major bilaterian taxa (Fig. 2F and fig. S3) and make up the major large patch of conserved surface in UNC-5 ectodomains (Fig. 2G).

Because heparin has been implicated in binding to several neuronal adhesion and signaling receptors, including other immunoglobulin superfamily proteins, we looked for structural clues in other IG-type receptors with heparin binding. Robo receptors, which are also repulsive guidance receptors, bind heparin using the same surface at their IG1-IG2 boundary (Fig. 2H) (*33*), suggesting a conserved or convergent site for heparin interactions among immunoglobulin superfamily neuronal receptors for heparin binding, although the exact binding poses of the heparin molecules may vary for different heparin-binding proteins.

Mutations at the heparin-binding site of UNC-5 can strengthen or weaken UNC-5–UNC-6 interactions

Through directed evolution and structural biology, we have identified a positively charged surface at the UNC-5 IG1-IG2 boundary, which interacts with heparin, and could be mutated to increase UNC-6 affinity. To confirm and extend these findings using orthogonal methods, we performed surface plasmon resonance (SPR) experiments with UNC-5 mutants for binding heparin and/or UNC-6. First, we showed that UNC-6–UNC-5 binding is weak with a K_d of ~46 μM as measured using biotinylated UNC-6ΔC captured on an SPR chip (Fig. 3A and fig. S4A). The N18K and N188K mutations on UNC-5 improve binding to UNC-6, in agreement with the results of our directed evolution experiments (Fig. 3A and fig. S4A). Next, we confirmed via SPR that UNC-5 binds heparin (Fig. 3C, fig. S4D). The UNC-5 N18K and N188K mutations, which are at the heparin binding site according to our crystal structure, improve heparin binding as expected, with the double N➔K UNC-5 mutant binding heparin with a 16-fold increase in affinity (K_d, 26 versus 1.7 μM) (Fig. 3C and fig. S4, D and E). We also observed that UNC-6ΔC binds heparin with much higher affinity (K_d = 0.04 μM) (Fig. 3D and fig. S4F).

We observed in our yeast display experiments that the UNC-5–UNC-6 affinity is drastically improved in the presence of heparin. We confirmed these results with SPR: UNC-5 binds UNC-6ΔC with a K_d of 1.2 μM in the presence of 0.31 μM heparin (5 μg/ml), an improvement of 39-fold compared to UNC-5–UNC-6ΔC binding in the absence of heparin (Fig. 3B and fig. S4B). At this heparin concentration (5 μg/ml), we expect that while UNC-6 molecules are in complex with heparin, free wild-type (WT) UNC-5 would be mostly unoccupied with heparin, and therefore, the complex formation is unlikely to be a result of heparin chain simply recruiting UNC-5. As the two Asn's at the IG1-IG2 boundary can be mutated to positively charged Lys to improve UNC-5 affinity for both heparin and UNC-6, we expect that UNC-5 binding to UNC-6 in the presence of heparin should also be improved with these mutations: UNC-5 ectodomains with N18K and N188K mutations bind UNC-6 more strongly in the presence of heparin (Fig. 3B and fig. S4B).

On the basis of our yeast display and structural work, we were also able to create partial loss-of-function UNC-5 mutants by mutating the two Asn residues to Glu's. UNC-5 ectodomain with either N18E or N188E mutations show weaker binding to heparin (Fig. 3C and fig. S4, D and E) and weaker binding to UNC-6 in the presence or absence of heparin (Fig. 3, A and B, and fig. S4, A and B), with an affinity 4- to 10-fold worse than the WT UNC-6–UNC-5 interaction in the presence of heparin and 1.6- to 1.8-fold worse in the absence of heparin (fig. S4C). Because mutations to the heparin-binding site of UNC-5 affect its ability to bind UNC-6 even in the absence of heparin, it is possible that our UNC-5 and/or UNC-6 samples might have carried with them some GAG or GAG-like molecules from expression in insect cells. Another explanation for this effect is that these mutations could induce conformational effects on the UNC-5 IG1-IG2 boundary that affect the nearby UNC-6 binding site (as revealed below).

While UNC-5 N➔E mutants have lower affinity for UNC-6 as expected, binding is not fully abolished due to the remaining extensive positive charge at the IG1-IG2 boundary of the UNC-5 ectodomain. On the basis of our crystal structure of the UNC-5–heparin complex, we designed four mutants of UNC-5, reversing charge at the heparin-binding site. Mutants contained a subset or all of the following amino acid substitutions: R17E, R70E, K11E, R190E, and R191E. All of the mutants showed a drastic reduction in heparin affinity, e.g., UNC-5 ectodomains with the double mutation R17E R70E lost heparin-binding affinity by >20-fold compared to WT (Fig. 4, A and B, and fig. S5, A and D). Binding to UNC-6, in the absence or presence of heparin, is also affected with all mutants, but only slightly when heparin is absent (Fig. 4C and fig. S5B), but to a much greater degree when heparin is present (Fig. 4E and fig. S5, C and E): For example, UNC-5 R17E R70E binds UNC-6ΔC in the presence of heparin (5 μg/ml) with a K_d of approximately 50 to 100 μM

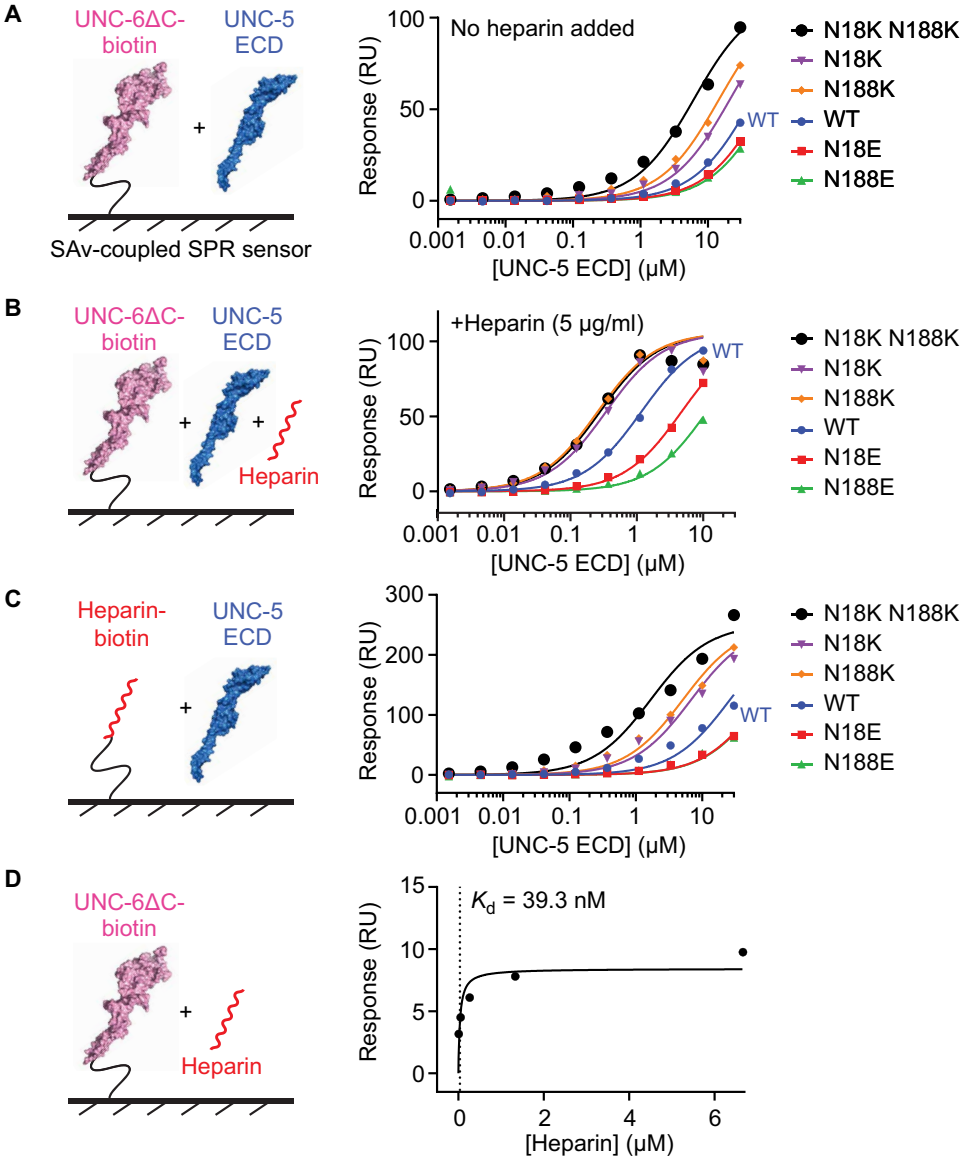

Fig. 3. UNC-5 mutations at N18 and N188 modulate UNC-5 affinity to UNC-6 and heparin. (**A** and **B**) Experimental design and binding isotherms for SPR experiments testing the interaction of biotinylated WT UNC-6ΔC with UNC-5 ECD WT and mutants without added heparin (A) and in the presence of heparin (5 μg/ml; B), where all UNC-5 variants (including WT) were run on the same SPR chip channel containing UNC-6ΔC within one experiment. Because many variants have very weak binding by design, we used the maximum saturation response values fit to the highest-affinity variant within each experiment as a constraint for fitting the lower-affinity variants. (**C**) Experimental design and binding isotherms for SPR experiments testing the interaction of biotinylated heparin with UNC-5 ECD WT and mutants, where all UNC-5 variants were run over a single heparin channel within one experiment. In all panels, N→K mutants increase affinity (left shift in the isotherms), while N→E decrease affinity. (**D**) Experimental design and binding isotherm for SPR experiment testing the interaction of biotinylated WT UNC-6ΔC with heparin. We measured UNC-6ΔC–heparin affinity with UNC-6 captured on the chip, because soluble UNC-6ΔC can best be used with a buffer containing $MgSO_4$ (see fig. S1B and Materials and Methods), which partly interferes with heparin binding. All sensorgrams for Fig. 3 are shown in fig. S4, and K_d's are tabulated in table S2.

(Fig. 4F). The mutations to the UNC-5 ectodomain modified affinity to both heparin and UNC-6, suggesting that the heparin-binding site of UNC-5 is near the UNC-6–binding site as well. Overall, these results imply that UNC-5 binding to heparin strongly facilitates UNC-6 binding and that there are additional weak contacts between UNC-5 and UNC-6 that are heparin independent, in agreement with the observation that UNC-5 binds UNC-6 weakly in the absence of heparin.

Heparin binding creates a large and stable repulsive netrin-receptor complex

Because heparin can bind both UNC-6/netrin and UNC-5 and increase their affinity to each other, we next asked the question whether we can reconstitute a stable extracellular complex of UNC-6 and UNC-5. In size exclusion chromatography (SEC) runs, we could not see a stable UNC-6ΔC–UNC-5 (extracellular domain) ECD complex without heparin (Fig. 5A), which is expected due to their low affinity in the absence

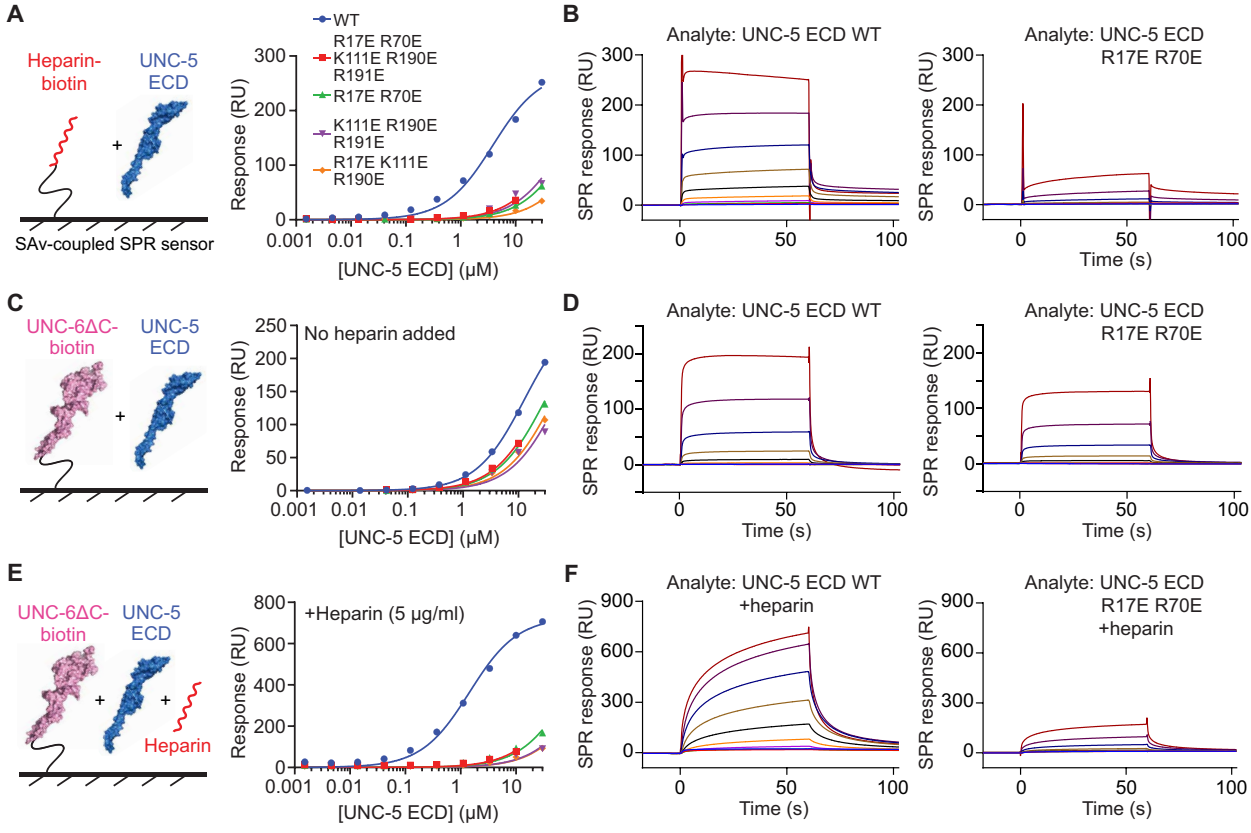

Fig. 4. Loss of heparin binding by UNC-5 accompanies loss of UNC-6 binding. (**A**) Experimental design (left) and binding isotherms (middle) for SPR experiments testing the interaction of biotinylated heparin with UNC-5 ECD WT and mutants, where all UNC-5 variants (including WT) were run over the same SPR chip channel containing heparin within one experiment. UNC-5 ECD mutants in Fig. 4 contain a subset or all of the following amino acid substitutions designed to disrupt heparin binding: R17E, R70E, K11E, R190E, and R191E. Because mutants bind very weakly by design, we used the maximum saturation response values fit to the highest-affinity variant within each experiment as a constraint for fitting the lower-affinity variants. (**B**) SPR sensorgrams for WT UNC-5 and the R17E R70E mutant in (A). See fig. S5 for all variants tested. (**C** and **E**) Experimental design (left) and binding isotherms (right) for SPR experiments testing the interaction of biotinylated WT UNC-6ΔC with UNC-5 ECD WT and mutants without heparin (C) and in the presence of heparin (5 μg/ml) (E). WT and mutant series were run on a single UNC-6ΔC channel on the SPR chip during the same experiment. (**D** and **F**) SPR sensorgrams for WT UNC-5 and the R17E R70E mutant in (B) and (C). See fig. S5 for all variants tested. K_d's are tabulated in table S3.

of heparin (Fig. 3A). When heparin (from porcine intestinal mucosa, ~16 kDa) was added at a 1:1:1.5 UNC-6:UNC-5:heparin molar ratio, a large stable complex was observed (Fig. 5B). The UNC-6–UNC-5–heparin complex peak elutes at 10.72 ml (~0.46 column volume) on a Superose 6 10/300 column, not at the void volume (7.20 ml; ~0.31 column volume) and well within the separation range of this column (up to 5 MDa). SDS–polyacrylamide gel electrophoresis (SDS-PAGE) analysis of the complex peak shows a complex including a roughly 1:1 molar ratio of UNC-6:UNC-5 (Fig. 5B and fig. S6A). In SEC runs, we have observed some UNC-5 and UNC-6 eluting much later than the complex peak: We observed this to be due to sulfate ions competing with heparin and preventing complex formation. We include magnesium sulfate in UNC-6ΔC preparations and in the SEC buffer to prevent nonspecific interactions of UNC-6 (see Materials and Methods).

We also hypothesized that the formation of the UNC-6–UNC-5 complex and its size may depend on the heparin polymer size and sulfation. Repeating the experiment with shorter heparin fragments results in smaller complexes and loss of the large complex peak on SEC runs (fig. S6B). Similarly, highly sulfated dextran sulfate and heparin were more effective in creating a large, oligomeric UNC-6–UNC-5 complex, while bulk HS, which is less sulfated, was much less effective (fig. S6C).

The presence of heparin and UNC-5 mostly excludes UNC-40 from an UNC-6 complex

It has been suggested that heparin binding might bias the binding of netrins toward specific receptors (*11*). If that is the case, we may expect heparin to weaken or break the otherwise stable UNC-6 complex with UNC-40/DCC. When UNC-6ΔC, UNC-5, and UNC-40 ECDs are mixed in the absence of heparin and applied to an SEC column, we could only observe this UNC-6–UNC-40 complex and free UNC-5 (Fig. 5C). However, when heparin is included in the mixture, we observed a very large complex peak containing UNC-6 and UNC-5 with a largely substoichiometric UNC-40 content and now free UNC-40 eluting much later (Figs. 5D and fig. S6A). This confirms that heparin and/or UNC-5 mostly competes with UNC-40 for UNC-6 binding. Because UNC-40 is also needed for some repulsive UNC-5–mediated functions (*8*, *10*, *34*), UNC-40 may contribute to repulsive signaling as part of a netrin–UNC-5 complex, probably at a lower stoichiometric ratio to not initiate attractive signaling. Removing heparin from this SEC run with three proteins resulted in the loss of the megadalton-sized complex peak, and formation of the attractive UNC-6–UNC-40 complex (Fig. 5C).

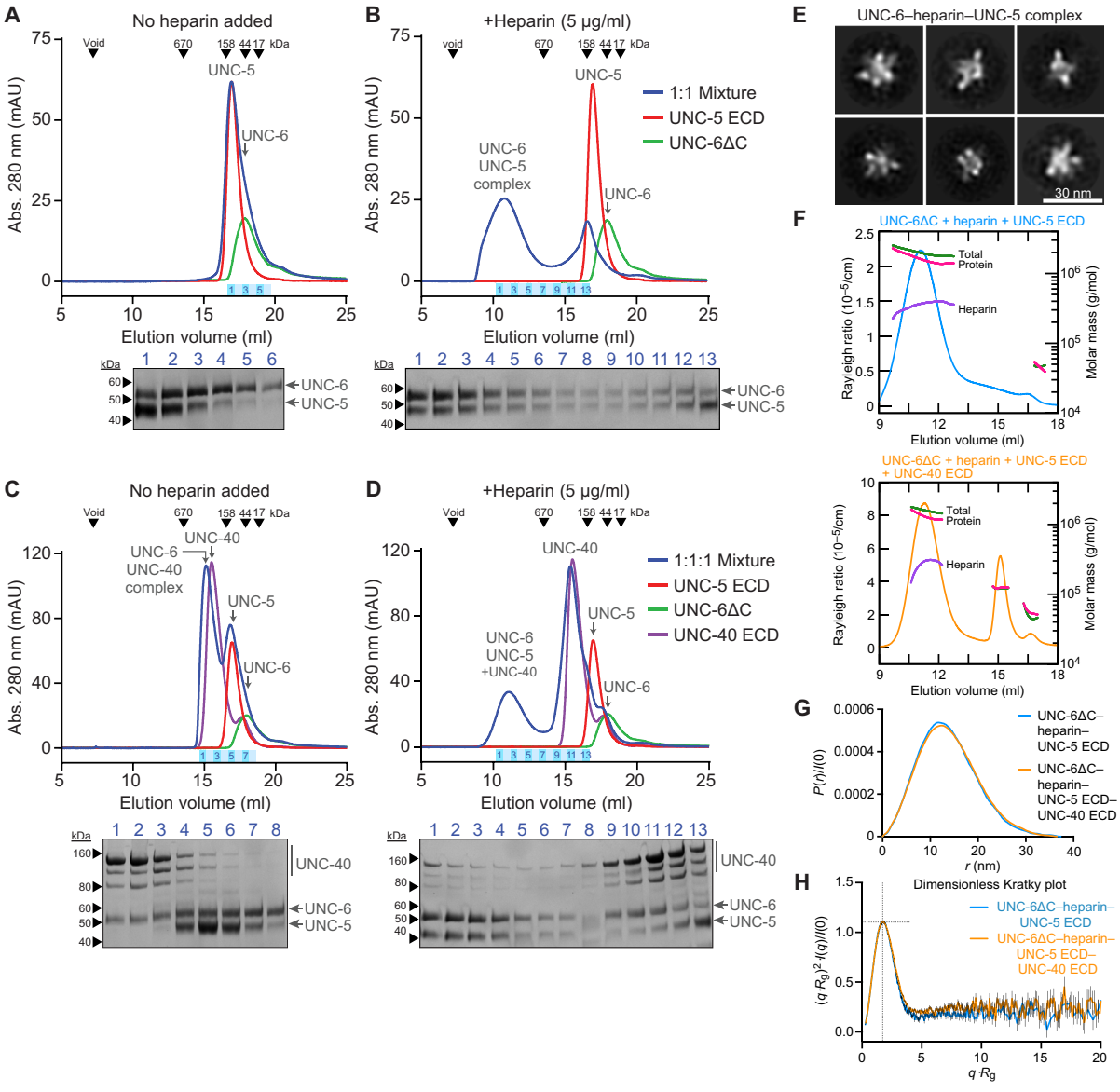

Fig. 5. UNC-5 and UNC-6 form a large oligomeric complex in the presence of heparin. (**A** and **B**) SEC for UNC-5 ECD and UNC-6ΔC. UNC-5 ECD (red), UNC-6ΔC (green), and a 1:1 molar mixture (blue) were injected without added heparin (A) and with heparin (5 μg/ml) (B) on a column equilibrated in HBS-MS and no heparin. Chromatograms in (A) to (D) show elution profiles measured by absorbance at 280 nm (path length = 0.2 cm) using a Superose 6 Increase 10/300 column, along with SDS-PAGEs of eluted fractions from the runs with mixtures (blue). Coomassie-stained bands are quantified in fig. S6A. (**C** and **D**) SEC for UNC-5 ECD, UNC-6ΔC, and UNC-40 ECD. UNC-5 ECD (red), UNC-6ΔC (green), UNC-40 ECD (purple), and a 1:1:1 molar mixture (blue) were injected without heparin (C) and with heparin (5 μg/ml) added (D) on a Superose 6 10/300 column equilibrated with HBS-MS. Coomassie-stained SDS-PAGEs for the mixture runs (blue) are placed under the chromatograms, and are quantified in fig. S6A. (**E**) Selected class averages of particles from negative-stained electron microscopy images for the UNC-6–heparin–UNC-5 complex. For raw images, see fig. S7A. (**F**) Molar mass measurements with conjugate analysis using SEC-MALS data for (top) UNC-6ΔC + heparin + UNC-5 ECD and (bottom) UNC-6ΔC + heparin + UNC-5 ECD + UNC-40 ECD. Blue and orange curves represent excess Rayleigh ratios, and green, magenta, and purple curves are molar mass measurements for total, protein, and conjugate (heparin) content, respectively. See table S4 for details. (**G**) Pair distribution plots for SAXS data, showing a mostly globular shape for the UNC-6–heparin–UNC-5 complex (blue) and the UNC-6–heparin–UNC-5–UNC-40 complex (orange). (**H**) Dimensionless Kratky plots. Dashed lines mark ($\sqrt{3}$,3/*e*) the expected maximum for a globular, rigid molecule. Additional SAXS analysis is shown in fig. S7 and table S5.

Similarly, additional SEC runs where UNC-6ΔC and UNC-40 ECD are mixed and loaded show that including heparin in the injected samples results in breaking the UNC-6–UNC-40 complex, with nearly all UNC-40 eluting as free protein, while mostly-UNC-6 oligomers are formed (fig. S6D). This further suggests that heparin or HS down-regulates formation of the attractive complex, while promoting the repulsive one.

Heparin-mediated UNC-6–UNC-5 oligomers are globular and relatively rigid

An important question relevant to UNC-5 signaling is (i) whether the heparin + UNC-6–mediated UNC-5 oligomers are an ordered and well-defined molecular species or (ii) whether these oligomers are simply a result of UNC-6 and UNC-5 decorating the long, linear

heparin chains. The two hypotheses may be distinguished on the basis of methods that measure shape and flexibility. We first used negative-staining electron microscopy to visualize the UNC-5–heparin–UNC-6 complex (Fig. 5E and fig. S7A). The images and class averages consistently show a large, globular complex, and not long or thin chains. We also used multiangle light scattering (MALS) and small-angle x-ray scattering (SAXS) to study these complexes in solution: Heparin, UNC-6ΔC, and UNC-5 ECD were mixed and injected onto an SEC column, and MALS and SAXS data were collected as the complex eluted. MALS data show that the complex is 1.5 to 2.0 MDa, and conjugate analysis of the complex peak indicates a substantial (~19%) presence of heparin (Fig. 5F and table S4). The pair distribution [$P(r)$] plot and the molecular shape analysis from the SAXS data both indicate a strongly globular complex, and the dimensionless Kratky plot confirms a highly rigid molecular species (Fig. 5G; fig. S7, B to F; and table S5). Given the inherent flexibility of the heparin chain, the multidomain nature of the proteins, including the flexible UNC-5 ectodomain (fig. S2A), and their elongated structures, this is not expected and indicates that the UNC-6–heparin–UNC-5 complex has a stable, ordered geometry and defined structure, which may be important for a signaling-competent conformation on the cell surface. The various mass and size measurements by MALS (Fig. 5F and table S4), SAXS (table S5), and comparison of the particle dimensions in electron micrographs (fig. S7A) and the SAXS $P(r)$ plots (Fig. 5G) show good agreement between the methods used. We also added the UNC-40 ECD to our SEC-MALS-SAXS samples of UNC-6ΔC + UNC-5 ECD + heparin (Fig. 5, F and G, and fig. S7, B to F): The substoichiometric UNC-40 ECD did not substantially affect the shape, flexibility, and structure of the UNC-5–heparin–UNC-6 complex.

Heparin-mediated oligomerization of UNC-6

We next investigated how the UNC-6–UNC-5 complex could oligomerize and hypothesized that this could be due to heparin-mediated oligomerization of UNC-6. To gain more insights into the UNC-6 structure, we were able to determine the structure of UNC-6ΔC, but not with heparin bound (Fig. 6A). However, we observed an ordered sulfate ion at a highly positively charged site on the second epidermal growth factor (EGF) domain of UNC-6 (Fig. 6B), close to where netrin–UNC-5 binding was proposed based on antibody-blocking experiments (*35*). The positive charge at this site is conserved in the monophyletic netrin-1/3/5 family of proteins but not in netrins that separately evolved and are not known to mediate axon guidance (i.e., netrin-4 and netrin-G families) (fig. S8A) (*10*, *36*). Finci *et al.* (*10*) have also observed putative sulfate ions in the human netrin-1–DCC crystal structure at the second EGF domain and proposed the positively charged surface on the EGF2 domain as a potential heparin-binding site.

To test whether the positively charged surface on EGF2 is the heparin-binding site outside the C-terminal NTR domain, we created and purified an UNC-6ΔC mutant where K354, R355, R357, R378, R404, and K405 were mutated to glutamate (fig. S8B). When WT UNC-6ΔC is run on an SEC column after being mixed with heparin at a 1:1.5 molar ratio, it runs as a large oligomer (Fig. 6C). This engineered UNC-6ΔC mutant ("heparin binding–deficient mutant"), however, does not oligomerize when mixed with heparin. We also performed SPR experiments to measure heparin affinity for WT and mutant UNC-6ΔC, where biotinylated heparin was captured on an SPR chip, and soluble UNC-6ΔC was used as an analyte at a variety of $MgSO_4$ concentrations to counter nonspecific binding (Fig. 6D and fig. S8C). The heparin-binding–deficient UNC-6ΔC mutant showed no binding, while we observed nanomolar to micromolar affinity for WT UNC-6ΔC depending on the $MgSO_4$ concentration in SPR buffer, in agreement with our measurements in Fig. 3D. As heparin can still bind and oligomerize WT UNC-6ΔC even in the presence of 100 mM SO_4^{2-} in SEC column running buffer, UNC-6ΔC is clearly a potent heparin-binding protein. Our results show that the positively charged site on the EGF2 domain is a heparin-binding site, which also helps oligomerize UNC-6 in the presence of heparin. Given these data, a plausible model for the formation of large UNC-6–UNC-5–heparin complexes is through heparin-mediated UNC-6 oligomerization.

Heparin-binding activity of UNC-5 is necessary for UNC-6–controlled dorsal migration of cells during development

To reveal whether a functional netrin–UNC-5 complex depends on the ability of UNC-5 to interact with heparin, we engineered one of our heparin binding–deficient UNC-5 mutants, R17E R70E, in *C. elegans*. Early studies have identified a requirement for UNC-6–UNC-5 signaling in dorsal guidance of both distal tip cells and motor axons. The two mobile distal tip cells, one leading the anterior gonad arm and one leading the posterior gonad arm, are the leading cells of the developing gonad that migrates along the ventral side of the animal before turning dorsally in hermaphrodites. These cells continue to migrate to the dorsal-most region of the animal before turning again to continue migration along the anterior-posterior axis (Fig. 7A) (*37*). The migration route of the distal tip cells establishes the U-shaped morphology of the gonads in the adult hermaphrodite (*38*). The dorsal migration requires both *unc-6* and *unc-5* (*8*), which is consistent with a repulsive action against a ventral source of UNC-6/netrin (*39*, *40*). In addition, the HSPG LON-2/Glypican modifies UNC-6–UNC-5 signaling in the migrating distal tip cells (*16*). We observed that in *unc-5(R17E R70E)* animals, distal tip cells regularly fail to turn dorsally or migrate the full length of the dorsal-ventral body axis (Fig. 7, B and C). The phenotype was much stronger for posterior distal tip cells, as previously observed in *unc-6* and *unc-5* mutants (*8*). We compared the phenotype from *unc-5(R17E R70E)* animals with mutant strains *unc-6(ev400)* and *unc-5(e53)*, previously identified as null mutants for dorsal migration-related functions (*8*). The failed distal tip cell migrations of *unc-5(R17E R70E)* mutants are indistinguishable from the defects observed in null *unc-6* and *unc-5* mutant animals for both anterior and posterior distal tip cells (Fig. 7C). These results indicate that netrin-dependent UNC-5 function requires the heparin-binding activity of UNC-5 during distal tip cell migration, as this is likely necessary for a stable, oligomeric, and functional UNC-6–UNC-5 complex. They also offer a possible mechanism for how the requirement for GAGs in distal tip cell migration arises (*41*, *42*).

Given the conserved role of UNC-6/UNC-5 signaling in axon repulsion, we next investigated whether UNC-5's interaction with heparin is necessary for growth cone guidance. We studied the circumferential axon guidance known to be mediated by UNC-5 and UNC-6, where ventrally localized UNC-6 repels UNC-5 expressing neuronal commissures toward the dorsal side of the animal (*8*). We found that the *unc-5(R17E R70E)* mutant animals showed normal axon guidance, suggesting that the UNC-5–heparin interaction is dispensable for the commissure axon guidance (Fig. 7, D to F). Consistent with the lack of morphological deficit of axon structures, these

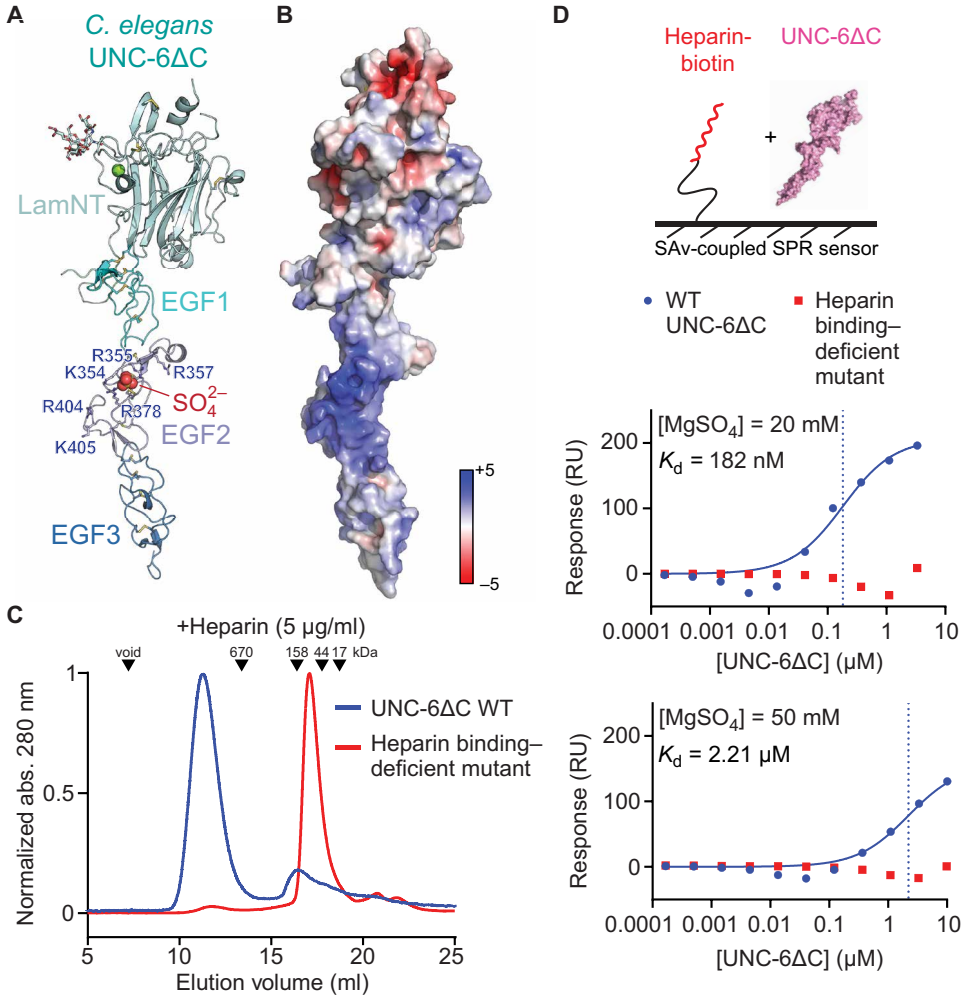

Fig. 6. UNC-6 EGF2 is a heparin-binding site. (**A** and **B**) Our crystal structure (A) and electrostatic potential surface (B) of UNC-6ΔC. The range of electrostatic potential used to color the surface is from −5 to +5 *kT/e*. (**C**) SEC of UNC-6ΔC WT (blue) and the heparin binding–deficient mutant (red) mixed with heparin (5 μg/ml). (**D**) Binding isotherms for SPR experiments testing the interaction of biotinylated heparin with UNC-6ΔC WT (blue) and the heparin-binding–deficient mutant (red) at two $MgSO_4$ concentrations to counter nonspecific binding. Sensorgrams are shown in fig. S8.

mutant animals also did not exhibit uncoordinated movement phenotype. Together, these data indicate that UNC-6/UNC-6/HS interactions dictate some repulsive guidance in vivo and that neurons may have compensatory mechanisms to overcome abrogated UNC-5/UNC-6/HS binding.

Disrupting UNC-5–UNC-6 protein contacts results in defects in repulsive axon guidance in *C. elegans*

Because no high-resolution structure of an UNC-5–UNC-6/netrin complex has been determined, we tested structure predictions using the recently released Alphafold-multimer (version 2.3.0) via the Colabfold implementation (*43*, *44*). We obtained a complex model with a strong interface predicted Template Modeling (ipTM) value of 0.79 (*43*, *45*), indicating a likely correct interface prediction (figs. S9, A to C). In the predicted model, the multiple UNC-6 domains make contact with UNC-5 IG2 (Fig. 8A), which is known to mediate this complex (*29*, *35*, *46*). Furthermore, the predicted model positions the positively charged heparin-binding surfaces of both proteins next to each other, creating a composite heparin-binding site (Fig. 8B), and is therefore in strong agreement with our model where an HS chain would strengthen a weak UNC-5–UNC-6 complex. To test the validity of the predicted model and create variants of UNC-5 that break UNC-5–UNC-6 protein-protein contacts, we tested mutations at this interface. UNC-5 mutants I159A S162A D163A, I167A S169A, and T127A Q129A could not effectively form complexes with UNC-6ΔC in the presence of heparin compared to WT UNC-5 when tested using SEC runs (Fig. 8C), although UNC-6ΔC oligomers can still form.

Next, we tested whether the protein-protein contacts within the UNC-5–UNC-6 complex are required for repulsive guidance in vivo. We engineered the UNC-5 mutation I159A S162A D163A into *C. elegans* using CRISPR-Cas9. Mutant larvae displayed a mild uncoordinated phenotype, matched by a partial defect in repulsive axon guidance in circumferential neurons that is weaker than the phenotype of *unc-5* null animals (Fig. 8, D and E). These mutants also had gonad morphology defects similar to the heparin binding–deficient mutants of UNC-5 (Fig. 8, F and G), despite the heparin-binding site being

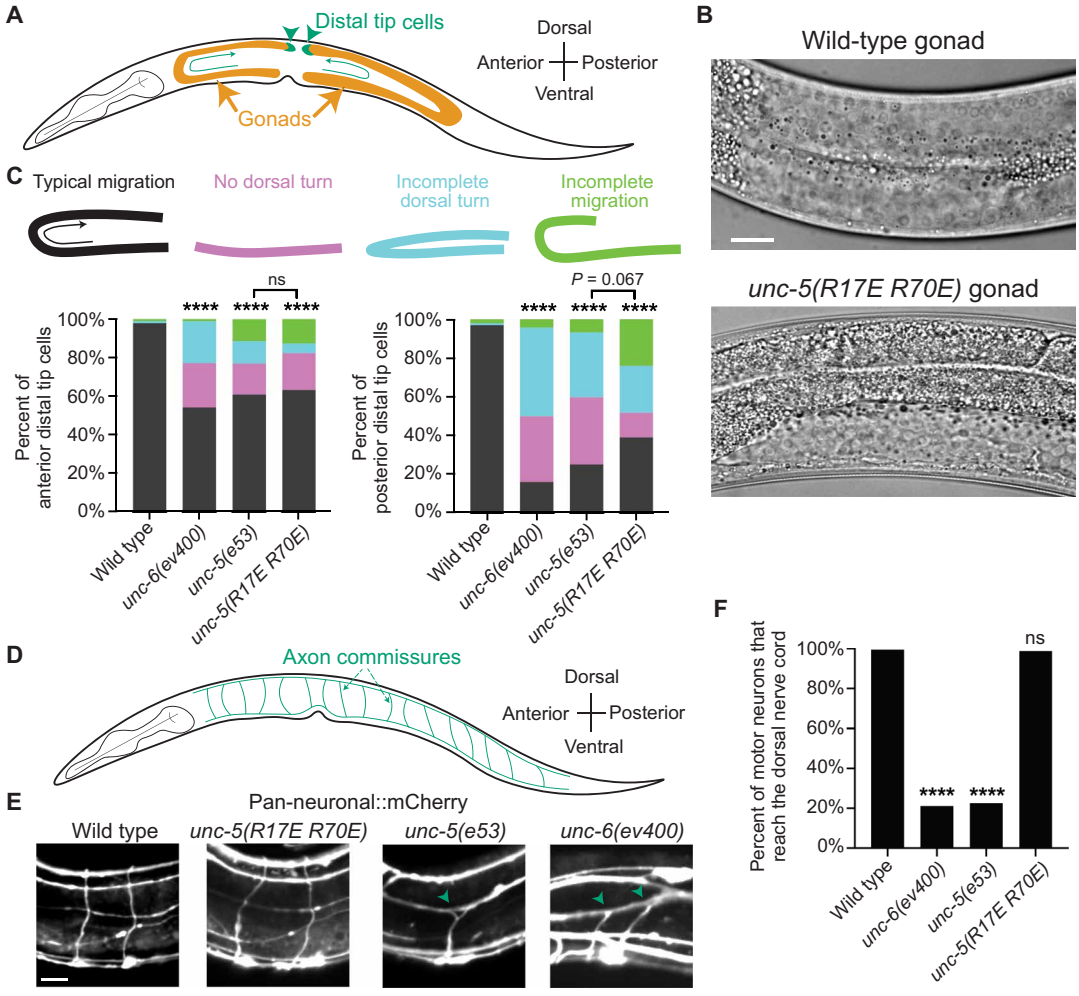

Fig. 7. Heparin binding is required for UNC-5–mediated cell migration. (**A**) Cartoon drawing of the *C. elegans* gonad. Gonad morphology (orange) is established by the migration of the distal tip cell (green). (**B**) DIC images of gonad morphology in WT and *unc-5(R17E R70E)* animals. Scale bar, 10 μm. (**C**) Quantification of distal tip cell migration phenotypes in WT ($n = 95$ animals), *unc-6(ev400)* ($n = 92$), *unc-5(e53)* ($n = 87$), and *unc-5(R17E R70E)* ($n = 79$) animals. Both *ev400* and *e53* are null alleles. Various phenotypes are observed: typical distal tip cell migration (black), a failed dorsal turn (magenta), a partial dorsal turn (blue), and incomplete longitudinal migration (green). The left graph represents anterior distal tip cells, and the right graph represents posterior distal tip cells. (**D**) Cartoon of the *C. elegans* motor axon commissures. Commissural axons migrate dorsally from the ventral nerve cord. (**E**) Confocal images of motor axon commissures in L2 *prab-3::mCherry* transgenic animals. Green arrowheads denote axons that fail to complete their dorsal longitudinal navigation. Scale bar, 10 μm. (**F**) Percentage of motor neurons in WT ($n = 13$ animals, 184 axons), *unc-6(ev400)* ($n = 13$ animals, 170 axons), *unc-5(e53)* ($n = 13$ animals, 209 axons), and *unc-5(R17E R70E)* ($n = 13$ animals, 171 axons) L2 animals that reach the dorsal nerve cord. Motor neurons in *unc-5(R17E R70E)* animals are able to navigate to the dorsal nerve cord. (C) and (F) use two-sided Fisher's exact tests. ****$P < 0.0001$.

intact. The severity of the *unc* phenotype in these mutants decreases with age, suggesting that the axon guidance deficits were ameliorated as development progresses. When we generated *unc-5* animals with UNC-6 nonbinding and heparin nonbinding mutations combined (R17E R70E I159A S162A D162A), they showed a strong uncoordinated phenotype in larvae and adults, as well as the distal tip cell migration defect (Fig. 8, F and G), indistinguishable from null *unc-5* animals. Circumferential motor axon guidance defects were observed in the combined mutant larvae at levels comparable to null *unc-5* animals (Fig. 8, D and E). Furthermore, these mutants demonstrated enhanced commissural axon guidance defects compared to mutant *unc-5* animals with only UNC-6 nonbinding mutations. These results show that the UNC-5–UNC-6 complex formed by weak protein-protein contacts is partially necessary for the axon guidance function of this complex in vivo, but heparin-binding provides an additive guidance function in UNC-5–mediated axon and cell migrations.

The three binding sites on netrin have different affinities

Structural studies on netrins and its receptors have previously focused on mammalian orthologs. To extend our findings to vertebrate netrins and its receptors and build on earlier structural findings, we next used structure-guided mutagenesis to study DCC and UNC5 binding sites on human netrin-1. Two crystal structures of soluble mammalian netrin-1ΔC constructs (previously named netrin-1s) in complex with different truncation constructs of DCC provide a composite view with three netrin-DCC binding sites (*9*, *10*), termed here sites 1, 2, and 3, from the N-to-C termini of netrin (Fig. 9A). We created a series of human netrin-1s constructs with point-mutant combinations so that

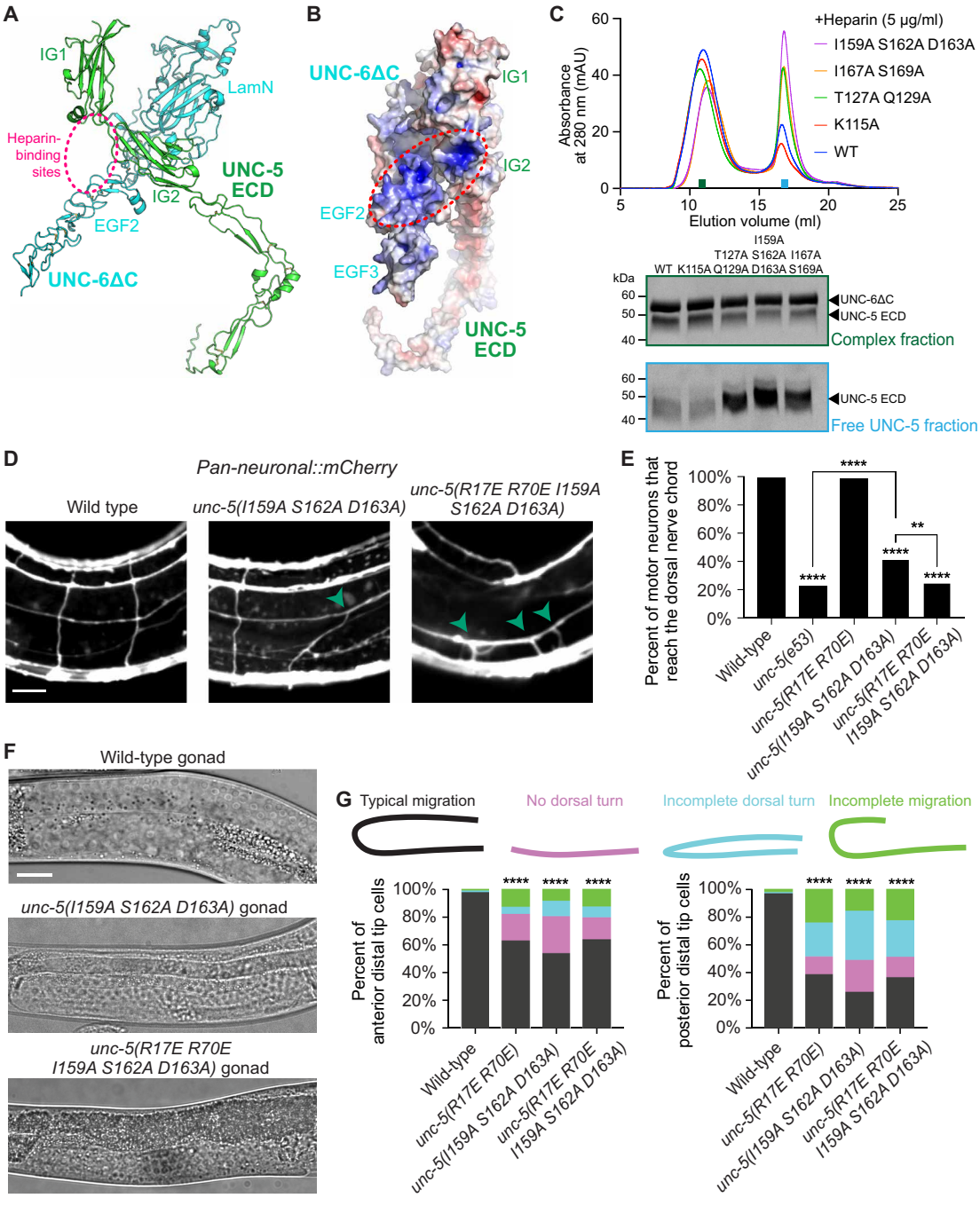

Fig. 8. Breaking UNC-6 contacts of UNC-5 results in cell migration and axon guidance phenotypes. (**A**) Highest-ranked Alphafold-multimer predicted model for UNC-6ΔC bound to UNC-5 ECD. See fig. S9 for details. (**B**) Electrostatic potential surface for the complex in rotated view, highlighting the contiguous positively charged surfaces we showed to bind heparin. (**C**) SEC runs (Superose 6 Increase 10/300, in HBS-MS) for UNC-6ΔC and heparin mixed with WT and mutant UNC-5. The mutants are designed at the Alphafold-predicted protein-protein contacts (see also fig. S9C). The SEC fractions analyzed with SDS-PAGE are labeled with green and blue rectangles. (**D**) Confocal images of motor axon commissures in L2 *prab-3::mCherry* transgenic animals. Green arrowheads denote axons that fail to complete their dorsal longitudinal navigation. Scale bar, 10 μm. (**E**) Percent of motor neurons in WT ($n = 13$ animals, 184 axons), *unc-5(e53)* ($n = 13$ animals, 209 axons), *unc-5(R17E R70E)* ($n = 13$ animals, 171 axons), *unc-5(I159A S162A D163A)* ($n = 13$ animals, 188 axons), and *unc-5(R17E R70E I159A S162A D163A)* ($n = 13$ animals, 170 axons) L2 animals. Loss of the UNC-5–HS interaction enhances motor axon dorsal migration defects in animals with disrupted UNC-5–UNC-6 binding. (**F**) DIC images of gonad morphology in WT, *unc-5(I159A S162A D163A), and unc-5(R17E R70E I159A S162A D163A)* animals. Scale bar, 10 μm. (**G**) Quantification of anterior (left) and posterior (right) distal tip cell migration phenotypes in WT ($n = 95$ animals), *unc-5(e53)* ($n = 87$), *unc-5(R17E R70E)* ($n = 79$), *unc-5(I159A S162A D163A)* ($n = 83$), and *unc-5(R17E R70E I159A S162A D163A)* ($n = 89$) animals. Various phenotypes are observed: typical distal tip cell migration (black), a failed dorsal turn (magenta), a partial dorsal turn (blue), and incomplete longitudinal migration (green). (E) and (G) use two-sided Fisher's exact tests. ****$P < 0.0001$ and **$P < 0.01$.

only one intact binding site remained per construct (Fig. 9, B and C): To eliminate DCC binding to site 1, a point mutation was introduced in the LamN domain (S148R). Binding to the other two sites on netrin-1 was abolished using mutations previously identified to be effective in axon guidance studies (*10*): DCC binding to site 2 was abolished with a double mutant (R348D R351D) in the EGF2 domain and binding to site 3 was abolished with a single point mutant in the EGF3 domain (Q445A). The resulting biotinylated netrin constructs were used in an AVEXIS (avidity-based extracellular interaction screening) assay (*47*), where netrin was bound to a streptavidin surface to measure binding to human draxin or with ectodomains, domain-specific truncations, or splice variants of human DCC and UNC5B, fused with β-lactamase and cartilage oligomeric matrix protein (COMP) pentamerization domains (Fig. 9D).

The binding assay showed that the netrin-1s mutant with zero intact sites (which has four point mutations in total) abolishes binding to DCC, UNC5B, and draxin, whereas the WT netrin-1s construct shows binding to all three proteins (Fig. 9E). The binding pattern of netrin-1s with the DCC ectodomain occurred with relative intensities so that site 1 > site 3 > site 2, indicating that the DCC binding site to the netrin LamN domain is the strongest as previously observed (Fig. 9E) (*9*). As expected from prior studies (*9*, *10*), the same binding pattern was seen whether the full ectodomain of DCC was used, or a truncated version covering domains FN4, FN5, and FN6 (FN456) as used in the crystal structures. In addition, we tested netrin binding for the splice variant of DCC that deletes a linker region between domains FN4 and FN5 ("FN456-short") that is the transiently dominant form of DCC during development of the mouse brain and neural tube, a feature that also appears conserved in humans (*48*–*50*). In our assay, this short splice variant of DCC abolishes binding specifically at site 3 (Fig. 9E). This agrees with the net reduced binding function of WT proteins in cell-based assays (*51*) and indicates specific alterations in the mechanism of netrin-DCC assembly for the splice variant. In keeping with past findings, draxin bound netrin only at site 3 (*52*), while UNC5B bound only at site 2 using its IG1 + 2 domains (*29*, *35*) in agreement with our *C. elegans* UNC-5–UNC-6 binding data above. Together, these binding data indicate that we have obtained the full structural scope of netrin-DCC binding, and that netrin site 1 binds strongly to DCC and may not be in competition with draxin or UNC5, whereas sites 2 and 3 are hotspots for variable interactions.

Heparin switches netrin-receptor selection at specific binding sites

We showed above that nematode UNC-6ΔC and UNC-5 interact strongly in the presence of heparin, and the UNC-5 and heparin compete with UNC-40/DCC binding to UNC-6/netrin. To test the hypothesis that GAGs may also play a direct and targeted role in mammalian netrin-receptor selection (*53*), we investigated binding patterns between the site-specific netrin-1 mutant series and the receptors DCC and UNC5B using AVEXIS. At 1 mg/ml concentrations, heparin produced striking changes to netrin-receptor binding patterns (Fig. 9F). Whereas DCC binding was weakened and nearly abolished at site 3, UNC5B binding was greatly strengthened at site 2. Site 1 was unaffected, in agreement with an absence of sulfate ion clusters at this site in netrin structures, indicating no heparin binding (Fig. 9C). The specific role of heparin to enhance the binding of

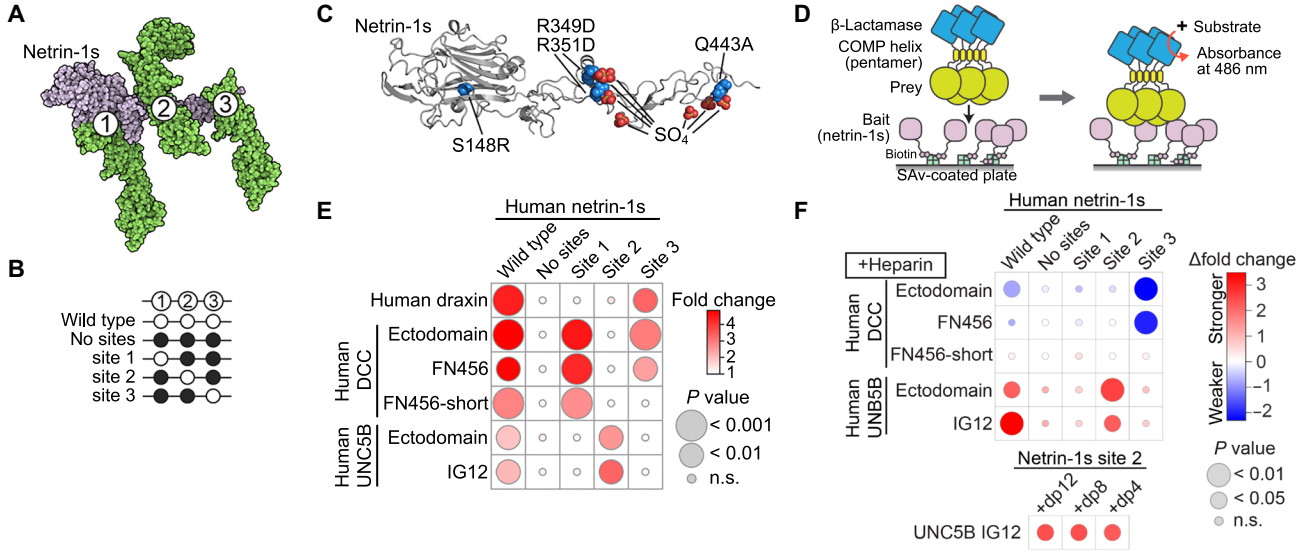

Fig. 9. Heparin enhances human UNC5B binding and suppresses DCC binding to netrin-1. (**A**) Composite binding model of netrin-1s (gray) with DCC (green) from available crystal structures reveals three binding sites (*9*, *10*). (**B**) Design of netrin mutants for which only one binding site is left intact (open circles) by mutating the remaining two binding sites (filled circles). (**C**) Mutations implemented (blue spheres) in netrin-1s (gray cartoon). Clusters of sulfate ions are depicted at sites 2 and 3 (red spheres). (**D**) Design of the AVEXIS assay. (**E**) Site-specific binding pattern of netrin to draxin, DCC, and UNC5B in an AVEXIS assay using HEK293 secreted proteins. DCC bound within its FN456 domain to netrin in series of intensity at site 1 > site 3 > site 2 (n.s., not significant in the dynamic range of this assay), whereas UNC5B bound within its IG1 + 2 domains to netrin at only site 2. A short DCC splice variant with 20-residue linker deletion between FN4 and FN5 abolishes binding specifically at site 3, while draxin binds predominantly at site 3. Fold change in binding signal is calculated relative to background signals of HEK293 media. (**F**) AVEXIS molecular assembly assay as performed in (E), with the addition of 1 mg/ml of naturally heterogeneous heparin (top) and purified heparin/HS compounds (bottom). The short heparin sulfate material used is from highly sulfated segments of heparin and comprises 4 to 12 saccharides of mainly trisulfated disaccharide units (IdoUA,2S-GlcNS,6S; approximately 75%). ΔFold change is the difference in fold change of binding signals over background upon addition of heparin or HS.

UNC5B IG1 + 2 at netrin-1 site 2 is also preserved with purified heparin/HS compounds of reduced polysaccharide length (dp4 to 12; Fig. 9F). Thus, binding in competitive netrin-receptor assemblies highlights a substantial equilibrium shift and switch in preference for UNC5B inclusion when HS is a cofactor.

DISCUSSION

The molecular environment of UNC-5–expressing neurites and cells controls their growth and migrations. In this study, we showed that GAGs regulate netrin–UNC-5 interactions and the processes controlled by them. We deciphered the set of interactions needed to create the netrin–heparin–UNC-5 complex, revealed how netrin–UNC-40 interactions may be controlled by GAGs, and show that disrupting interactions between UNC-5 and GAGs causes morphological defects during development. We further demonstrated that UNC-5–mediated repulsive guidance requires UNC-5 contacts with both GAGs and UNC-6.

First, we showed experimentally that UNC-5 is a heparin-binding protein. Our structural and biophysical results implicate the boundary of the IG1 and IG2 domains of UNC-5 in its interactions with HS. UNC-5 mutations that break HS and HS-mediated UNC-6 binding also cause small but consistent loss of binding to UNC-6 in the absence of heparin. These findings are supported by previous results showing that the IG domains are necessary and sufficient for binding between human netrin-1 and UNC5C (*29*, *46*) and mouse netrin-1 and UNC5H2 (*35*).

We present a model of an UNC-6–heparin–UNC-5 complex that is very large yet well ordered. For this, we demonstrated that the EGF2 domain of UNC-6/netrin is a heparin-binding site, and heparin can oligomerize UNC-6 through this secondary interaction site, even in the absence of its C-terminal NTR domain, which was identified as the primary heparin interaction site previously (*21*). Our findings on the EGF2 domain are compatible with previous biochemical studies, which had implicated the netrin EGF2 domain in netrin–UNC-5 interactions (*35*, *46*), and EGF2 as a potential HS-binding site was recognized (*10*) but had not been shown. Our work also suggests that multiple domains of UNC-6 (LamN, EGF1, and EGF2) may be involved in protein-protein contacts with UNC-5, which explains previous observations that the repulsive guidance activity of UNC-5 and binding to netrin may be mediated by many domains of UNC-6 (*46*, *54*).

It is reasonable to assume that the length of the linear heparin/HS chains helps determine the size of the megadalton-sized UNC-6 oligomers and the UNC-6–UNC-5 complex, and our SAXS data also strongly point to a globular and rigid complex. Considering not only the flexibility of linear heparin chains but also the direct protein-protein contacts between UNC-6 and UNC-5 (which we could break with specific mutations), we propose that such a rigid and large complex has to form via a combination of protein-protein and protein-glycan contacts. This composite model of interactions to form netrin–UNC-5 complexes is appealing, as the specificity of binding would best be provided by protein-protein (UNC-6–UNC-5) contacts, and interactions with heparin/HS provide much of the binding energy for the formation of the UNC-6–UNC-5 complex.

While we favor a model where UNC-6–UNC-5 contacts provide specificity for turning on UNC-5–mediated repulsive signaling, our data comparing different sulfoglycans suggest that the distribution and frequency of sulfation domains on HS polymers and HS length may be important factors for the formation of UNC-5–UNC-6 complexes or oligomers. While we did not test this, it is also possible that additional interactions with the polypeptide chain of an HSPG can regulate UNC-5 actions and contribute to specificity in vivo. This last possibility may be true for an attractive netrin receptor, *C. elegans* UNC-40/DCC, which was shown to interact with the polypeptide chain of the HSPG LON-2/glypican (*16*).

Because heparin and HS molecules are long, linear chains of sulfated glycans, one such molecule can usually bind more than one protein ligand. However, as we are adding a molar equivalent or excess heparin to UNC-6 or UNC-5 + UNC-6 in our experiments, we had expected a majority of UNC-6–heparin or UNC-6–UNC-5–heparin complexes to include one or two protein chains bound to one heparin molecule, rather than very large complexes in the megadalton size range. Our observations, therefore, suggest that UNC-6 alone or the UNC-6–UNC-5 complex can oligomerize on heparin chains in a cooperative manner, which further supports the model that protein-protein contacts within UNC-6–UNC-6 and UNC-6–UNC-5 oligomers are crucial to support large oligomer formation, in addition to necessary protein contacts with heparin.

Netrins present a binding hub, due to their multifunctional sites 2 and 3. We previously showed that draxin remodels netrin-receptor assembly to elicit distinct cellular behaviors (*55*) and demonstrate here that this concept could be further generalized with other netrin "cofactors," such as HS. Our results support the hypothesis that GAGs play a more direct and targeted role in netrin-receptor selection that is reminiscent of the variable roles of HS and various GAGs in other neuronal receptor signaling mechanisms (*53*). It is also possible that a specific HS moiety may bind more potently than other segments along the chain, and the length of an HS chain increases the probability of its occurrence.

We also attempted to reconstitute the UNC-6–UNC-5–UNC-40 complex, which had been observed before in pull-down experiments (*34*) but not successfully at scale. We observed that heparin can inhibit interactions between nematode and mammalian UNC-6/netrin and UNC-40/DCC. When we mixed UNC-5, UNC-6, UNC-40, and heparin, we observed UNC-40 on the large oligomer, but only at a largely substoichiometric ratio, probably mediated by UNC-6–UNC-40 interactions using site 1 on UNC-6, which is free of heparin and UNC-5 contacts. This observation supports the hypothesis that UNC-5 and/or heparin might at least partly compete for UNC-40/DCC binding on UNC-6/netrin (*11*), which has functional consequences: Repulsive signaling may require UNC-40/DCC to not strongly cluster, which would otherwise lead to attractive signaling, but still be present in a complex with highly clustered UNC-5 molecules for a repulsive outcome. The competition model, where UNC-5 and heparin displace UNC-40/DCC from UNC-6/netrin, was previously proposed in a functional setting, where UNC-5 outcompeting DCC on site 2 on netrin results in axon repulsion, in agreement with our model (*10*).

In addition to structural insights, we were able to use the molecular reagents we engineered, i.e., UNC-5 variants, to directly ask the following functional question: Is the UNC-5–heparin interaction we discovered necessary for the in vivo functions UNC-5 performs, especially those that are UNC-6 dependent? We created animals with the heparin nonbinding mutation UNC-5 R17E R70E, which has lost its UNC-6ΔC affinity by >40-fold in the presence of heparin, but only ~2-fold in the absence of heparin, compared to WT UNC-5. These animals displayed gonadal morphology defects comparable to *unc-5*

and *unc-6* null animals (*8*), supporting our in vitro results and structural data on identifying the UNC-5–heparin interaction site and the functional importance of this interaction.

Previous studies have reported that cell migration defects, including several mesodermal cells, such as the distal tip cells in the gonad, are accompanied by dorsal axon guidance phenotypes in *unc-5* and *unc-6* mutant animals (*8*). We have observed that when UNC-5 is no longer able to interact with HS but retains its weak UNC-6 affinity, the two phenotypes can be separated: Distal tip cell migration is fully altered as in null *unc-5* or *unc-6* animals, while axon guidance toward the dorsal nerve chord is not affected. This observation may be explained by several mechanisms: (i) UNC-5–mediated cell migrations may depend on the higher affinity of HS-mediated UNC-6–UNC-5 interactions, while a weaker affinity in the absence of HS is sufficient for axon guidance functions as a result of different dosage dependence in the two systems, or (ii) the presence of HSPGs and HS-mediated oligomerization of the UNC-6–UNC-5 complex is necessary for signaling during distal tip cell migrations. It is speculative but possible that HSPG interactions allow for haptotactic responses where UNC-6/netrin is immobilized on an HSPG substrate, which could then be required during distal tip cell migration.

Furthermore, we were able to characterize direct UNC-6–UNC-5 contacts using an Alphafold-predicted model. Only when we broke both UNC-6 and heparin/HS contacts of UNC-5 could we reproduce a full cell migration and axon guidance phenotype as observed in *unc-5* or *unc-6* null animals.

We also engineered UNC-5 to bind heparin with higher affinity than WT: It would be interesting to see whether higher HS affinity would allow this UNC-5 variant (N18K N118K) to respond to UNC-6 at lower doses or at lower-density tracks of HSPGs, resulting in premature dorsal cell migrations in vivo. Recent transcriptomic analyses of *C. elegans* neurons have revealed low, but detectable, levels of *unc-5* transcript in neurons that do not rely on UNC-5 signaling for proper axon outgrowth (*56*). As such, in vivo mutations that increase HS affinity may also phenocopy axon migration defects after UNC-5 overexpression in touch receptor neurons. In these neurons, ectopic expression of UNC-5 was shown to reroute axons toward the dorsal region of the animal (*39*).

During the review of our manuscript, two articles were released that complement our findings on the roles of proteoglycans and GAGs in netrin and/or UNC-5 function. Meier *et al.* (*57*) observed that vertebrate netrins oligomerize with heparin through interactions with their EGF2 domains, similar to our findings with UNC-6, and breaking this interaction in the nematode model results in the distal tip cell migration phenotype as we have shown for UNC-5. Akkermans *et al.* (*58*) showed that mouse UNC5D can form oligomers with a glypican, but without contacting the HS chain. These studies further highlight the need to study neurite and cell migration within the context of surrounding proteoglycans and other relevant cofactors in vivo.

Last, our biochemical and structural findings are also in line with the large body of available functional data, beyond our own in vivo results. It was observed that milder phenotypes of *unc*-5 partial loss-of-function mutants are sensitized in the background of glypican and syndecan mutations, and the repulsive guidance and cell migration actions of UNC-5 depend on LON-2/glypican, functionally linking HSPGs to UNC-5 function (*14*, *16*). The UNC-6 EGF2 domain was identified as essential to UNC-5–mediated functions, as the deletion of the EGF2 domain results in complete loss of repulsive guidance and migration functions (*8*, *54*), and R➔A mutations on the EGF2 domain causes netrin-1 to lose its UNC5-mediated anti-apoptopic effect (*35*). Last, mutants designed to misfold the IG1 domain of UNC-5 show distal tip cell migration phenotypes and axon guidance effects, although some of the other domain disruptions had similar effects (*58*). Our work here establishes a model that provides molecular explanations for the extensive netrin literature, while enabling future studies using engineered molecules and structural models we have generated, and may serve as a stepping stone toward an atomic-resolution structure of the complete repulsive signaling complex.

MATERIALS AND METHODS

Protein expression and purification for *C. elegans* proteins

All *C. elegans* proteins were expressed using the baculoviral expression system and the lepidopteran High Five cell line in Insect-XPRESS (Lonza, catalog no. BELN12-730Q). Baculoviruses were produced using homologous recombination in insect cells by co-transfection with linearized baculoviral DNA and the transfer vector pAcGP67A (BD Biosciences), which carries an N-terminal gp64 signal peptide for secretion. All proteins were tagged C-terminally with a hexahistidine tag for purification. When indicated, some constructs were tagged C-terminally with a BirA recognition sequence (GLNDIFEAQKIEWHE), for facile enzymatic biotinylation, followed by a hexahistidine tag. Biotinylation was performed using the BirA ligase reaction kit (Avidity, catalog no. BirA500).

UNC-5, UNC-6, and UNC-40 constructs of various lengths were purified first with Ni–nitrilotriacetic acid metal-affinity chromatography (QIAGEN, catalog no. 30210) from conditioned media, followed by SEC with either Superose 6 Increase 10/300 (GE Healthcare, catalog no. 29-0915-96) or Superdex 200 Increase 10/300 columns (GE Healthcare, catalog no. 28-9909-44). UNC-5 and UNC-40 are purified in 10 mM Hepes (pH 7.2) and 150 mM NaCl [Hepes-buffered saline (HBS)], while UNC-6ΔC may exhibit aggregation and stickiness to chromatography resin, as recently recognized by Krahn *et al.* (*60*). We tested numerous buffer conditions in SEC experiments and observed that UNC-6ΔC (A22-P461) is soluble in a buffer with 500 mM NaCl and shows excellent SEC elution profiles and complete protein recovery when in 10 mM Hepes (pH 7.2), 150 mM NaCl, and 100 mM $MgSO_4$ (HBS-MS), presumably as magnesium acting as a chaotrope and sulfate interacting with the heparin-binding site(s) (fig. S1B).

Yeast surface display

All yeast clones and libraries were made using electrically competent EBY100 yeast (Thermo Fisher Scientific, catalog no. 83900) (*61*). UNC-5 ECD, containing 2 Ig and 2 Tsp1 domains, was displayed on yeast via fusion of the C terminus of UNC-5 ECD to the N terminus of Aga2. A Myc-tag was included on the C terminus of UNC-5 for quantification of fusion protein expression via staining with an Alexa Fluor 488–coupled anti-myc (Thermo Fisher Scientific, catalog no. MA1-980-A488). To test binding to UNC-6 of yeast displaying UNC-5, an UNC-6 construct lacking the C-terminal NTR domain, known to cause aggregation, and containing a BirA biotin ligase recognition sequence was expressed and purified (UNC-6ΔC). A yeast staining reagent was created by biotinylating UNC-6ΔC and incubating it with Alexa Fluor 647 (Thermo Fisher Scientific, catalog no. A20347)–coupled streptavidin.

The UNC-5 ECD display library was created using random error-prone mutagenesis. Separation of yeast populations was done via magnetic-activated cell sorting (Miltenyi Biotec, catalog no. 130-091-051) using either streptavidin (Miltenyi Biotec, catalog no. 130-048-101) or anti–Alexa Fluor 647 microbeads (Miltenyi Biotec, catalog no. 130-091-395). Progress during selections was assessed by UNC-6ΔC binding and monitored using flow cytometry on a BD Accuri C6 flow cytometer.

The yeast library underwent three rounds of selection, performed in decreasing concentrations of heparin from porcine intestinal mucosa (Sigma-Aldrich Heparin Grade I-A, catalog no. H3149). The first round was performed with streptavidin microbeads in 400 nM UNC-6ΔC monomers and heparin (4 μg/ml). The second round was performed with anti–Alexa Fluor 647 microbeads in 125 nM UNC-6ΔC monomers and heparin (0.062 μg/ml). The third round was performed the same as the second round, excluding heparin.

Individual yeast clones (96 total) were isolated after the third selection round. These clones were tested for their ability to bind UNC-6ΔC. Of the 96 clones, 8 higher-affinity clones were chosen for further analysis. Binding affinities to UNC-6ΔC on yeast without added heparin were measured and the DNA sequence of UNC-5 ECD was sequenced for each clone. Apparent affinities from protein-binding experiments on yeast were measured by plotting control-subtracted mean fluorescence intensities on binding isotherms using a one-site, specific binding model in Prism version 9 (GraphPad).

Protein crystallization

A construct containing the first two IG domains of *C. elegans* UNC-5 with a C-terminal hexahistidine tag was purified as described above and concentrated to 25 mg/ml in HBS. Crystals were grown with the sitting-drop vapor diffusion method and using microseeding to improve single crystal growth in the crystallant 1.25 M $(NH_4)_2SO_4$, 0.1 M tris (pH 8.5), and 0.2 M Li_2SO_4 at 22°C. Cryoprotection was achieved using a cryoprotectant supplemented with 30% glycerol by flash-freezing in liquid nitrogen.

UNC-5 IG1-2 with the short heparin fragment dp4 (degree of polymerization, 4) (Iduron, catalog no. HO04; molecular weight, ~1.2 kDa) was crystallized after mixing purified protein with dp4 at a 1:3 molar ratio. Crystallization was achieved with UNC-5 (20 mg/ml) using vapor diffusion with the hanging-drop method with the crystallant 4% (v/v) pentaerythritol ethoxylate (3/4 EO/OH), 0.1 M sodium acetate (pH 4.6), 16% (w/v) polyethylene glycol (PEG) 8000, and 0.2 M NaCl at 22°C. Crystals were cryoprotected in 0.1 M sodium acetate (pH 4.8), 16% PEG 8000, 0.2 M NaCl, 25% ethylene glycol, and dp4 (60 μg/ml) by flash-freezing in liquid nitrogen.

UNC-6ΔC with a C-terminal hexahistidine tag was purified over Superdex 200 10/300 after being mixed with heparin-dp16 (Iduron, catalog no. HO16; molecular weight, ~4.65 kDa) at a 1:1.5 molar ratio in the HBS-MS buffer. Protein was concentrated to 12 mg/ml; we could not check whether any dp16 was carried over during purification and concentration. Crystallization was achieved using hanging-drop vapor diffusion with 0.1 M tris (pH 8.0) and 10% (w/v) PEG 8000 at 22°C. Crystals were cryoprotected with 0.1 M tris (pH 8), 10% PEG 8000, 30% glycerol, and dp16 (0.12 mg/ml). We did not observe any electron density for any heparin-like molecules, as crystal packing appears to be blocking much of our predicted HS-binding site, except for an ordered putative sulfate ion (present at 100 mM in the protein buffer).

Structure determination by x-ray crystallography

Crystallographic data were indexed, merged, and scaled using the XDS package (*62*). Molecular replacement was performed with Phaser (*63*) in the Phenix package (*64*). The UNC-5 IG1 + 2 structure was solved using the structure of the human Unc5A ectodomain (*30*) with domains 1 and 2 as separate molecular replacement models [Protein Data Bank (PDB) ID: 4V2A] after homology modeling for the *C. elegans* sequences with MODELLER (*65*). The structure with heparin-dp4 was determined using our UNC-5 IG1 + 2 structure as the molecular replacement model. The UNC-6ΔC structure was solved using the AlphaFold model as the molecular replacement model (*66*). The program phenix.refine was used to refine the model structure in reciprocal space (*67*), and Coot was used for model building and correction in real space (*68*). Model building and refinement was guided by MolProbity tools within Phenix for checking chemical geometry (*69*).

The diffraction data for the UNC-5 IG1 + 2 with heparin-dp4 crystals were highly anisotropic (see table S1 for details). This dataset was reduced using the XDS package and then ellipsoidically truncated and anisotropically corrected using the STARANISO server (*70*). STARANISO-corrected structure factors were used during refinement.

During model building for our UNC-6 structure, we came across density corresponding to a metal ion previously identified as calcium in other netrin structures. Because our protein was dissolved in 100 mM $MgSO_4$, it is possible that the calcium ion may or may not have been replaced by a magnesium ion during purification; the resolution of the structure does not allow for a definitive identification.

For analysis of sequence and structural features, we heavily used the Adaptive Poisson-Boltzmann Solver (APBS) plug-in in PyMOL for electrostatic potential surface calculations (*71*) and ConSurf for calculating sequence conservation (*72*). Isoelectric points and extinction coefficients were calculated using the Protparam server (*73*).

Surface plasmon resonance

A Biacore T200 (GE Healthcare) at 22°C was used to measure the binding affinities by the equilibrium method, as kinetics of binding was too fast to measure in most occasions. Biotinylated UNC-6ΔC or heparin (Millipore Sigma, catalog no. 375054) was captured on a streptavidin-coated sensor chip (Cytiva, catalog no. 29104992). Analytes for biotinylated UNC-6ΔC included UNC-5 ECD [with and without heparin (5 μg/ml)] and heparin. Analytes for biotinylated heparin included UNC-5 ECD and UNC-6ΔC. The running buffer for all SPR experiments was 10 mM Hepes (pH 7.2), 150 mM NaCl, 0.05% Tween 20, and 0.1% bovine serum albumin, supplemented with either 20 or 50 mM $MgSO_4$ when UNC-6ΔC was an analyte to reduce nonspecific binding. A regeneration step was performed after each injection using 10 mM Hepes (pH 7.2), 150 mM NaCl, 0.05% Tween 20, and 100 mM $MgSO_4$. Titration series were performed once for each mutant/variant, each time with 9 to 10 measurement points.

Using Biacore evaluation software, the K_d was calculated by fitting the equilibrium data with a 1:1 binding model, whenever binding was observed to nearly saturate. Supplemental tables list the K_d values and the SE of the fit. With mutants that had very low affinities, saturation of the sensor surface was practically impossible. The SPR experiments were performed by running WT and point mutants on the same SPR channel within the same titration series, where we did not observe any notable loss of activity (i.e., binding response to same analyte) over

many runs. This has allowed us to use R_{max} values (SPR response at saturation) from the highest-affinity variant as constraints for approximate K_d predictions for weak mutants in Prism (GraphPad version 9). Because of the inability to reach near saturation values, the calculated K_d values at >50 μM should be considered not accurate.

Negative-staining electron microscopy

UNC-5 ECD and UNC-6ΔC were expressed and purified as described above. The proteins were mixed at a 1:1 molar ratio in the presence of heparin (5 μg/ml; ~16 kDa) to facilitate complex formation. The protein mixture was then run over an SEC column, Superose 6 Increase 10/300 (GE Healthcare, catalog no. 29-0915-96) in HBS-MS. A fraction from the complex peak was diluted to 8 μg/ml and used for grid preparation. The UNC-6-heparin-UNC-5 sample was pipetted onto 400-mesh carbon-coated copper grids (Electron Microscopy Sciences, CF400-CU) and excess solution was blotted. The sample was stained twice with 1% (w/v) uranyl acetate and allowed to fully dry.

The negative-stain grid was imaged at room temperature with a FEI Tecnai F30 electron microscope at 300 kV at the Advanced Electron Microscopy Facility in University of Chicago. A total of 25 images were recorded at ×49,000 magnification. From those images, 7812 particles were picked manually with a final pixel size of 3.12 Å. RELION-3.0.8 was used for all image processing (*74*).

Multiangle light scattering and small-angle x-ray scattering

MALS and SAXS data were collected at the APS beamline 18-ID using a Superose 6 10/300 column on the SEC-MALS-SAXS setup. The protein samples were prepared by mixing UNC-6ΔC, UNC-5 ECD, and UNC-40 ECD at molar equal ratios with heparin at 1.5 times the molar equivalent. No heparin was present in the running buffers. Detailed experimental conditions and analysis parameters are listed in table S4 for MALS and in table S5 for SAXS. MALS data were collected on a DAWN HELIOS II MALS equipment with an Optilab T-rEX dRI detector (Wyatt Technology). For the UNC-6ΔC–heparin–UNC-5 ECD–UNC-40 ECD complex, we used a sheath coflow strategy (buffer: HBS) to remedy radiation damage (*75*). SAXS data were processed in BioXTAS RAW version 2.1.4 (*76*), using tools from the ATSAS package, version 3.1.3 (*77*, *78*), and several molecular weight estimation methods implemented within RAW (*79*–*81*). For the UNC-6–heparin–UNC-5 data, we used evolving factor analysis (EFA) deconvolution as implemented in RAW to extract scattering from the complex and not the isolated components as a precaution (*82*). However, analysis of frames corresponding to just those collected for the major peak gave similar results to those we report using EFA in table S5.

Generation of mutant *C. elegans* with CRISPR-Cas9 and phenotypic analysis of animals

C. elegans were grown at 20°C on NGM plates and fed with *Escherichia coli* according to standard procedures (*83*). N2 Bristol was used as the WT reference strain. The following additional strains were used in this study: wyIs371 V (TV12310), *unc-6(ev400)* X; wyIs371 V (TV28935), *unc-5(e53)* IV; wyIs371 V (TV12715), *unc-5(wy1796)* VI; wyIs371 V (TV28567), *unc-5(I59A S162A D163A) VI;* wyIs371 V and *unc-5(R17E R70E I59A S162A D163A) VI;* and wyIs371 V.

Base pair mutations in *unc-5* were generated by microinjections of CRISPR-Cas9 protein complexes in N2 Bristol animals. Genome editing using CRISPR-Cas9 was carried out by standard protocols (*84*). Cas9 protein and tracRNA (Integrated DNA Technologies) were injected at a concentration of 1.525 μM each. CRISPR RNAs (crRNAs; IDT) were injected at a concentration of 1.525 μM. Single-stranded DNA repair templates were ordered as oligomers (Thermo Fisher Scientific) and injected at 6.67 μM. pRF6(*rol-6(su1006)*) was used as a coinjection marker and selected against after confirmation of a successful genome edit. Confirmation of genome edits was performed by sequencing of F_2 animals. The R17E and R70E edits were generated sequentially. The R17E mutation was generated with the following crRNA sequence: CUUAUUUUCAAUGACAUAAC. The R70E mutation was generated with the following crRNA sequence: GAAUCGACGUAGACACAUC. The I159A, S162A, and D163A mutations were generated using the following crRNA sequence: UUAGACUUCCAUCAGAUGCU.

C. elegans hermaphrodites in the late L4 and young adult stages were screened for gonad morphology and distal tip cell migration. Animals were anesthetized using 6 mM levamisole (Sigma-Aldrich) in M9 buffer and mounted on 4% agarose pads. Differential interference contrast (DIC) images were captured using an inverted Zeiss Axio Observer Z1 microscope equipped with a Yokogawa CSU-W1 spinning-disk unit and a Prime 95B Scientific complementary metal oxide semiconductor camera (Photometrics). Slidebook software (3i) was used to control imaging. A water-immersion C-Apochromat 40× 0.9–numerical aperture objective was used for all imaging. The same protocol was used on hermaphrodite worms in the L2 stage to screen for motor axon guidance. All images were processed using ImageJ/Fiji (National Institutes of Health) (*85*).

Expression and purification of human proteins

Our human netrin-1s construct comprised residues 25 to 453, lacking the native N-terminal signal peptide and the C-terminal NTR domain, to enhance expression and solubility. Human draxin was full length. Human DCC ectodomain was C-terminally truncated at the single-pass transmembrane segment. Human DCC FN456 (containing fibronectin type III domains 4 to 6) comprised residues 719 to 1098 and the shortened splice variant had an internal deletion of residues 819 to 838. Human UNC5B ectodomain was C-terminally truncated at the single-pass transmembrane segment, and UNC5B IG12 (IG domains 1 and 2) comprised residues 46 to 246. Mutations were introduced by QuikChange site-directed mutagenesis.

Molecular assembly assays (AVEXIS)

Netrin-1s was subcloned with C-terminal fusion to CD4 and a biotinylation target sequence (bait vector) (*47*). Other constructs were subcloned with C-terminal fusion to CD4, COMP, and β-lactamase (prey vector) (*47*). AVEXIS assays were performed as previously described (*52*, *55*). Briefly, human embryonic kidney (HEK) 293F cells were used for transient expression, biotinylation of bait protein, and secretion into media. Target protein levels were normalized, bait protein was incubated and washed on streptavidin-coated plates (Thermo Fisher Scientific, 436014), prey protein was incubated and washed along with any additives (heparin in Fig. 9), and prey β-lactamase activity was measured by absorbance at 486 nm with nitrocerfin as substrate (EMD Millipore, 484400). Experiments were repeated at least three times and included independent sample preparations. We used commercial preparations for heparin (porcine intestinal mucosa, Sigma-Aldrich, H3393) and short heparin/HS compounds that were purified from highly sulfated regions of heparin [Iduron, catalog nos. H004 (dp4), H008 (dp8), and H012 (dp12)].

Raw absorbance readings were converted to a fold-change ratio, i.e., experimental absorbance values were divided by the background absorbance values obtained when using HEK293 secretion media in the absence of netrin-1s expression. With additives in AVEXIS (specifically, heparin in Fig. 9), Δfold change was calculated as the difference in fold-change ratios ± additives. Statistics were performed with a Student's *t* test.

Supplementary Materials

This PDF file includes:

Figs. S1 to S9
Tables S1 to S5

REFERENCES AND NOTES

1. A. L. Kolodkin, M. Tessier-Lavigne, Mechanisms and molecules of neuronal wiring: A primer. *Cold Spring Harb. Perspect. Biol.* **3**, a001727 (2011).
2. Y. Zang, K. Chaudhari, G. J. Bashaw, New insights into the molecular mechanisms of axon guidance receptor regulation and signaling. *Curr. Top. Dev. Biol.* **142**, 147–196 (2021).
3. E. Cortés, J. S. Pak, E. Özkan, Structure and evolution of neuronal wiring receptors and ligands. *Dev. Dyn.* **252**, 27–60 (2023).
4. N. P. Boyer, S. L. Gupton, Revisiting netrin-1: One who guides (axons). *Front. Cell. Neurosci.* **12**, 221 (2018).
5. S. Y. Ko, C. R. Dass, K. Nurgali, Netrin-1 in the developing enteric nervous system and colorectal cancer. *Trends Mol. Med.* **18**, 544–554 (2012).
6. M. Brisset, M. Grandin, A. Bernet, P. Mehlen, F. Hollande, Dependence receptors: New targets for cancer therapy. *EMBO Mol. Med.* **13**, e14495 (2021).
7. B. Ramkhelawon, E. J. Hennessy, M. Ménager, T. D. Ray, F. J. Sheedy, S. Hutchison, A. Wanschel, S. Oldebeken, M. Geoffrion, W. Spiro, G. Miller, R. McPherson, K. J. Rayner, K. J. Moore, Netrin-1 promotes adipose tissue macrophage retention and insulin resistance in obesity. *Nat. Med.* **20**, 377–384 (2014).
8. E. M. Hedgecock, J. G. Culotti, D. H. Hall, The *unc-5*, *unc-6*, and *unc-40* genes guide circumferential migrations of pioneer axons and mesodermal cells on the epidermis in *C. elegans*. *Neuron* **4**, 61–85 (1990).
9. K. Xu, Z. Wu, N. Renier, A. Antipenko, D. Tzvetkova-Robev, Y. Xu, M. Minchenko, V. Nardi-Dei, K. R. Rajashankar, J. Himanen, M. Tessier-Lavigne, D. B. Nikolov, Neural migration. Structures of netrin-1 bound to two receptors provide insight into its axon guidance mechanism. *Science* **344**, 1275–1279 (2014).
10. L. I. Finci, N. Krüger, X. Sun, J. Zhang, M. Chegkazi, Y. Wu, G. Schenk, H. D. T. Mertens, D. I. Svergun, Y. Zhang, J. Wang, R. Meijers, The crystal structure of netrin-1 in complex with DCC reveals the bifunctionality of netrin-1 as a guidance cue. *Neuron* **83**, 839–849 (2014).
11. R. Meijers, R. G. Smock, Y. Zhang, J.-H. Wang, Netrin synergizes signaling and adhesion through DCC. *Trends Biochem. Sci.* **45**, 6–12 (2020).
12. T. Serafini, T. E. Kennedy, M. J. Galko, C. Mirzayan, T. M. Jessell, M. Tessier-Lavigne, The netrins define a family of axon outgrowth-promoting proteins homologous to *C. elegans* UNC-6. *Cell* **78**, 409–424 (1994).
13. Y. Matsumoto, F. Irie, M. Inatani, M. Tessier-Lavigne, Y. Yamaguchi, Netrin-1/DCC signaling in commissural axon guidance requires cell-autonomous expression of heparan sulfate. *J. Neurosci.* **27**, 4342–4350 (2007).
14. S. Gysi, C. Rhiner, S. Flibotte, D. G. Moerman, M. O. Hengartner, A network of HSPG core proteins and HS modifying enzymes regulates netrin-dependent guidance of D-type motor neurons in *Caenorhabditis elegans*. *PLOS One* **8**, e74908 (2013).
15. D. C. Merz, G. Alves, T. Kawano, H. Zheng, J. G. Culotti, UNC-52/perlecan affects gonadal leader cell migrations in *C. elegans* hermaphrodites through alterations in growth factor signaling. *Dev. Biol.* **256**, 173–186 (2003).
16. C. R. Blanchette, P. N. Perrat, A. Thackeray, C. Y. Bénard, Glypican is a modulator of netrin-mediated axon guidance. *PLOS Biol.* **13**, e1002183 (2015).
17. M. Brankatschk, B. J. Dickson, Netrins guide *Drosophila* commissural axons at short range. *Nat. Neurosci.* **9**, 188–194 (2006).
18. S. W. Moore, N. Biais, M. P. Sheetz, Traction on immobilized netrin-1 is sufficient to reorient axons. *Science* **325**, 166 (2009).
19. S. G. Varadarajan, J. H. Kong, K. D. Phan, T.-J. Kao, S. C. Panaitof, J. Cardin, H. Eltzschig, A. Kania, B. G. Novitch, S. J. Butler, Netrin1 produced by neural progenitors, not floor plate cells, is required for axon guidance in the spinal cord. *Neuron* **94**, 790–799.e3 (2017).
20. S. W. Moore, X. Zhang, C. D. Lynch, M. P. Sheetz, Netrin-1 attracts axons through FAK-dependent mechanotransduction. *J. Neurosci.* **32**, 11574–11585 (2012).
21. J. Kappler, S. Franken, U. Junghans, R. Hoffmann, T. Linke, H. W. Müller, K. W. Koch, Glycosaminoglycan-binding properties and secondary structure of the C-terminus of netrin-1. *Biochem. Biophys. Res. Commun.* **271**, 287–291 (2000).
22. Y. S. Lim, S. Mallapur, G. Kao, X. C. Ren, W. G. Wadsworth, Netrin UNC-6 and the regulation of branching and extension of motoneuron axons from the ventral nerve cord of *Caenorhabditis elegans*. *J. Neurosci.* **19**, 7048–7056 (1999).
23. K. Keino-Masu, M. Masu, L. Hinck, E. D. Leonardo, S. S. Chan, J. G. Culotti, M. Tessier-Lavigne, Deleted in colorectal cancer (DCC) encodes a netrin receptor. *Cell* **87**, 175–185 (1996).
24. E. D. Leonardo, L. Hinck, M. Masu, K. Keino-Masu, S. L. Ackerman, M. Tessier-Lavigne, Vertebrate homologues of *C. elegans* UNC-5 are candidate netrin receptors. *Nature* **386**, 833–838 (1997).
25. S.-A. Hussain, M. Piper, N. Fukuhara, L. Strochlic, G. Cho, J. A. Howitt, Y. Ahmed, A. K. Powell, J. E. Turnbull, C. E. Holt, E. Hohenester, A molecular mechanism for the heparan sulfate dependence of slit-robo signaling. *J. Biol. Chem.* **281**, 39693–39698 (2006).
26. A. N. Fox, K. Zinn, The heparan sulfate proteoglycan syndecan is an in vivo ligand for the *Drosophila* LAR receptor tyrosine phosphatase. *Curr. Biol.* **15**, 1701–1711 (2005).
27. K. G. Johnson, A. P. Tenney, A. Ghose, A. M. Duckworth, M. E. Higashi, K. Parfitt, O. Marcu, T. R. Heslip, J. L. Marsh, T. L. Schwarz, J. G. Flanagan, D. Van Vactor, The HSPGs Syndecan and Dallylike bind the receptor phosphatase LAR and exert distinct effects on synaptic development. *Neuron* **49**, 517–531 (2006).
28. E. L. Shipp, L. C. Hsieh-Wilson, Profiling the sulfation specificities of glycosaminoglycan interactions with growth factors and chemotactic proteins using microarrays. *Chem. Biol.* **14**, 195–208 (2007).
29. B. V. Geisbrecht, K. A. Dowd, R. W. Barfield, P. A. Longo, D. J. Leahy, Netrin binds discrete subdomains of DCC and UNC5 and mediates interactions between DCC and heparin. *J. Biol. Chem.* **278**, 32561–32568 (2003).
30. E. Seiradake, D. del Toro, D. Nagel, F. Cop, R. Härtl, T. Ruff, G. Seyit-Bremer, K. Harlos, E. C. Border, A. Acker-Palmer, E. Y. Jones, R. Klein, FLRT structure: Balancing repulsion and cell adhesion in cortical and vascular development. *Neuron* **84**, 370–385 (2014).
31. V. A. Jackson, S. Mehmood, M. Chavent, P. Roversi, M. Carrasquero, D. Del Toro, G. Seyit-Bremer, F. M. Ranaivoson, D. Comoletti, M. S. P. Sansom, C. V. Robinson, R. Klein, E. Seiradake, Super-complexes of adhesion GPCRs and neural guidance receptors. *Nat. Commun.* **7**, 11184 (2016).
32. J. Stetefeld, M. D. McDougall, P. C. Loewen, A. Moya, M. Meier, RCSB PDB - 6OOL: Structural elucidation of the Ectodomain of mouse UNC5H2 (2020); https://doi.org/10.2210/pdb6OOL/pdb.
33. N. Fukuhara, J. A. Howitt, S.-A. Hussain, E. Hohenester, Structural and functional analysis of slit and heparin binding to immunoglobulin-like domains 1 and 2 of *Drosophila* Robo. *J. Biol. Chem.* **283**, 16226–16234 (2008).
34. K. Hong, L. Hinck, M. Nishiyama, M. M. Poo, M. Tessier-Lavigne, E. Stein, A ligand-gated association between cytoplasmic domains of UNC5 and DCC family receptors converts netrin-induced growth cone attraction to repulsion. *Cell* **97**, 927–941 (1999).
35. M. Grandin, M. Meier, J. G. Delcros, D. Nikodemus, R. Reuten, T. R. Patel, D. Goldschneider, G. Orriss, N. Krahn, A. Boussouar, R. Abes, Y. Dean, D. Neves, A. Bernet, S. Depil, F. Schneiders, K. Poole, R. Dante, M. Koch, P. Mehlen, J. Stetefeld, Structural decoding of the netrin-1/UNC5 interaction and its therapeutical implications in cancers. *Cancer Cell* **29**, 173–185 (2016).
36. L. Leclère, F. Rentzsch, Repeated evolution of identical domain architecture in metazoan netrin domain-containing proteins. *Genome Biol. Evol.* **4**, 883–899 (2012).
37. E. M. Hedgecock, J. G. Culotti, D. H. Hall, B. D. Stern, Genetics of cell and axon migrations in *Caenorhabditis elegans*. *Development* **100**, 365–382 (1987).
38. J. E. Kimble, J. G. White, On the control of germ cell development in *Caenorhabditis elegans*. *Dev. Biol.* **81**, 208–219 (1981).
39. M. Hamelin, Y. Zhou, M. W. Su, I. M. Scott, J. G. Culotti, Expression of the UNC-5 guidance receptor in the touch neurons of *C. elegans* steers their axons dorsally. *Nature* **364**, 327–330 (1993).
40. W. G. Wadsworth, H. Bhatt, E. M. Hedgecock, Neuroglia and pioneer neurons express UNC-6 to provide global and local netrin cues for guiding migrations in *C. elegans*. *Neuron* **16**, 35–46 (1996).
41. T. Kinnunen, Z. Huang, J. Townsend, M. M. Gatdula, J. R. Brown, J. D. Esko, J. E. Turnbull, Heparan 2-O-sulfotransferase, hst-2, is essential for normal cell migration in *Caenorhabditis elegans*. *Proc. Natl. Acad. Sci. U.S.A.* **102**, 1507–1512 (2005).
42. N. Suzuki, H. Toyoda, M. Sano, K. Nishiwaki, Chondroitin acts in the guidance of gonadal distal tip cells in *C. elegans*. *Dev. Biol.* **300**, 635–646 (2006).
43. R. Evans, M. O'Neill, A. Pritzel, N. Antropova, A. Senior, T. Green, A. Žídek, R. Bates, S. Blackwell, J. Yim, O. Ronneberger, S. Bodenstein, M. Zielinski, A. Bridgland, A. Potapenko, A. Cowie, K. Tunyasuvunakool, R. Jain, E. Clancy, P. Kohli, J. Jumper, D. Hassabis, Protein complex prediction with AlphaFold-Multimer. bioRxiv 2021.10.04.463034 [Preprint] (2022). https://doi.org/10.1101/2021.10.04.463034.
44. M. Mirdita, K. Schütze, Y. Moriwaki, L. Heo, S. Ovchinnikov, M. Steinegger, ColabFold: Making protein folding accessible to all. *Nat. Methods* **19**, 679–682 (2022).

45. R. Yin, B. Y. Feng, A. Varshney, B. G. Pierce, Benchmarking AlphaFold for protein complex modeling reveals accuracy determinants. *Protein Sci.* **31**, e4379 (2022).
46. R. P. Kruger, J. Lee, W. Li, K.-L. Guan, Mapping netrin receptor binding reveals domains of Unc5 regulating its tyrosine phosphorylation. *J. Neurosci.* **24**, 10826–10834 (2004).
47. K. M. Bushell, C. Söllner, B. Schuster-Boeckler, A. Bateman, G. J. Wright, Large-scale screening for novel low-affinity extracellular protein interactions. *Genome Res.* **18**, 622–630 (2008).
48. M. A. Reale, G. Hu, A. I. Zafar, R. H. Getzenberg, S. M. Levine, E. R. Fearon, Expression and alternative splicing of the deleted in colorectal cancer (DCC) gene in normal and malignant tissues. *Cancer Res.* **54**, 4493–4501 (1994).
49. H. M. Cooper, P. Armes, J. Britto, J. Gad, A. F. Wilks, Cloning of the mouse homologue of the deleted in colorectal cancer gene (mDCC) and its expression in the developing mouse embryo. *Oncogene* **11**, 2243–2254 (1995).
50. J. C. Leggere, Y. Saito, R. B. Darnell, M. Tessier-Lavigne, H. J. Junge, Z. Chen, NOVA regulates Dcc alternative splicing during neuronal migration and axon guidance in the spinal cord. *eLife* **5**, e14264 (2016).
51. L. I. Finci, J. Zhang, X. Sun, R. G. Smock, R. Meijers, Y. Zhang, J. Xiao, J.-H. Wang, Structure of unliganded membrane-proximal domains FN4-FN5-FN6 of DCC. *Protein Cell* **8**, 701–705 (2017).
52. X. Gao, U. Metzger, P. Panza, P. Mahalwar, S. Alsheimer, H. Geiger, H.-M. Maischein, M. P. Levesque, M. Templin, C. Söllner, A floor-plate extracellular protein-protein interaction screen identifies draxin as a secreted netrin-1 antagonist. *Cell Rep.* **12**, 694–708 (2015).
53. R. G. Smock, R. Meijers, Roles of glycosaminoglycans as regulators of ligand/receptor complexes. *Open Biol.* **8**, 180026 (2018).
54. Y. Lim, W. G. Wadsworth, Identification of domains of netrin UNC-6 that mediate attractive and repulsive guidance and responses from cells and growth cones. *J. Neurosci.* **22**, 7080–7087 (2002).
55. Y. Liu, T. Bhowmick, Y. Liu, X. Gao, H. D. T. Mertens, D. I. Svergun, J. Xiao, Y. Zhang, J.-H. Wang, R. Meijers, Structural basis for draxin-modulated axon guidance and fasciculation by netrin-1 through DCC. *Neuron* **97**, 1261–1267.e4 (2018).
56. S. R. Taylor, G. Santpere, A. Weinreb, A. Barrett, M. B. Reilly, C. Xu, E. Varol, P. Oikonomou, L. Glenwinkel, R. McWhirter, A. Poff, M. Basavaraju, I. Rafi, E. Yemini, S. J. Cook, A. Abrams, B. Vidal, C. Cros, S. Tavazoie, N. Sestan, M. Hammarlund, O. Hobert, D. M. Miller, Molecular topography of an entire nervous system. *Cell* **184**, 4329–4347.e23 (2021).
57. M. Meier, M. Gupta, S. Akgül, M. McDougall, T. Imhof, D. Nikodemus, R. Reuten, A. Moya-Torres, V. To, F. Ferens, F. Heide, G. P. Padilla-Meier, P. Kukura, W. Huang, B. Gerisch, M. Mörgelin, K. Poole, A. Antebi, M. Koch, J. Stetefeld, The dynamic nature of netrin-1 and the structural basis for glycosaminoglycan fragment-induced filament formation. *Nat. Commun.* **14**, 1226 (2023).
58. O. Akkermans, C. Delloye-Bourgeois, C. Peregrina, M. Carrasquero-Ordaz, M. Kokolaki, M. Berbeira-Santana, M. Chavent, F. Reynaud, R. Raj, J. Agirre, M. Aksu, E. S. White, E. Lowe, D. Ben Amar, S. Zaballa, J. Huo, I. Pakos, P. T. N. McCubbin, D. Comoletti, R. J. Owens, C. V. Robinson, V. Castellani, D. Del Toro, E. Seiradake, GPC3-Unc5 receptor complex structure and role in cell migration. *Cell* **185**, 3931–3949.e26 (2022).
59. M. Killeen, J. Tong, A. Krizus, R. Steven, I. Scott, T. Pawson, J. Culotti, UNC-5 function requires phosphorylation of cytoplasmic tyrosine 482, but its UNC-40-independent functions also require a region between the ZU-5 and death domains. *Dev. Biol.* **251**, 348–366 (2002).
60. N. Krahn, M. Meier, R. Reuten, M. Koch, J. Stetefeld, T. R. Patel, Solution structure of *C. elegans* UNC-6: A nematode paralogue of the axon guidance protein netrin-1. *Biophys. J.* **116**, 2121–2130 (2019).
61. G. Chao, W. L. Lau, B. J. Hackel, S. L. Sazinsky, S. M. Lippow, K. D. Wittrup, Isolating and engineering human antibodies using yeast surface display. *Nat. Protoc.* **1**, 755–768 (2006).
62. W. Kabsch, XDS. *Acta Crystallogr. D Biol. Crystallogr.* **66**, 125–132 (2010).
63. A. J. McCoy, R. W. Grosse-Kunstleve, P. D. Adams, M. D. Winn, L. C. Storoni, R. J. Read, Phaser crystallographic software. *J. Appl. Cryst.* **40**, 658–674 (2007).
64. D. Liebschner, P. V. Afonine, M. L. Baker, G. Bunkóczi, V. B. Chen, T. I. Croll, B. Hintze, L. W. Hung, S. Jain, A. J. McCoy, N. W. Moriarty, R. D. Oeffner, B. K. Poon, M. G. Prisant, R. J. Read, J. S. Richardson, D. C. Richardson, M. D. Sammito, O. V. Sobolev, D. H. Stockwell, T. C. Terwilliger, A. G. Urzhumtsev, L. L. Videau, C. J. Williams, P. D. Adams, Macromolecular structure determination using x-rays, neutrons and electrons: Recent developments in Phenix. *Acta Crystallogr. D Struct. Biol.* **75** (Pt. 10), 861–877 (2019).
65. B. Webb, A. Sali, Comparative protein structure modeling using MODELLER. *Curr. Protoc. Bioinformatics* **54**, 5.6.1-5.6.37 (2016).
66. M. Varadi, S. Anyango, M. Deshpande, S. Nair, C. Natassia, G. Yordanova, D. Yuan, O. Stroe, G. Wood, A. Laydon, A. Žídek, T. Green, K. Tunyasuvunakool, S. Petersen, J. Jumper, E. Clancy, R. Green, A. Vora, M. Lutfi, M. Figurnov, A. Cowie, N. Hobbs, P. Kohli, G. Kleywegt, E. Birney, D. Hassabis, S. Velankar, AlphaFold protein structure database: Massively expanding the structural coverage of protein-sequence space with high-accuracy models. *Nucleic Acids Res.* **50**, D439–D444 (2022).
67. P. V. Afonine, R. W. Grosse-Kunstleve, N. Echols, J. J. Headd, N. W. Moriarty, M. Mustyakimov, T. C. Terwilliger, A. Urzhumtsev, P. H. Zwart, P. D. Adams, Towards automated crystallographic structure refinement with *phenix.refine*. *Acta Crystallogr. D Biol. Crystallogr.* **68**, 352–367 (2012).
68. P. Emsley, B. Lohkamp, W. G. Scott, K. Cowtan, Features and development of *Coot*. *Acta Crystallogr. D Biol. Crystallogr.* **66**, 486–501 (2010).
69. V. B. Chen, W. B. Arendall, J. J. Headd, D. A. Keedy, R. M. Immormino, G. J. Kapral, L. W. Murray, J. S. Richardson, D. C. Richardson, MolProbity: All-atom structure validation for macromolecular crystallography. *Acta Crystallogr. D Biol. Crystallogr.* **66**, 12–21 (2010).
70. I. J. Tickle, C. Flensburg, P. Keller, W. Paciorek, A. Sharff, C. Vonrhein, G. Bricogne, STARANISO, Global Phasing Ltd. (2018); https://staraniso.globalphasing.org/cgi-bin/staraniso.cgi.
71. E. Jurrus, D. Engel, K. Star, K. Monson, J. Brandi, L. E. Felberg, D. H. Brookes, L. Wilson, J. Chen, K. Liles, M. Chun, P. Li, D. W. Gohara, T. Dolinsky, R. Konecny, D. R. Koes, J. E. Nielsen, T. Head-Gordon, W. Geng, R. Krasny, G.-W. Wei, M. J. Holst, J. A. McCammon, N. A. Baker, Improvements to the APBS biomolecular solvation software suite. *Protein Sci.* **27**, 112–128 (2018).
72. H. Ashkenazy, S. Abadi, E. Martz, O. Chay, I. Mayrose, T. Pupko, N. Ben-Tal, ConSurf 2016: An improved methodology to estimate and visualize evolutionary conservation in macromolecules. *Nucleic Acids Res.* **44**, W344–W350 (2016).
73. E. Gasteiger, C. Hoogland, A. Gattiker, S. Duvaud, M. R. Wilkins, R. D. Appel, A. Bairoch, Protein identification and analysis tools on the ExPASy server, in *The Proteomics Protocols Handbook*, J. M. Walker, Ed. (Humana Press, 2005), pp. 571–607; https://doi.org/10.1385/1-59259-890-0:571.
74. J. Zivanov, T. Nakane, B. O. Forsberg, D. Kimanius, W. J. Hagen, E. Lindahl, S. H. Scheres, New tools for automated high-resolution cryo-EM structure determination in RELION-3. *eLife* **7**, e42166 (2018).
75. N. Kirby, N. Cowieson, A. M. Hawley, S. T. Mudie, D. J. McGillivray, M. Kusel, V. Samardzic-Boban, T. M. Ryan, Improved radiation dose efficiency in solution SAXS using a sheath flow sample environment. *Acta Crystallogr. D. Struct. Biol.* **72**, 1254–1266 (2016).
76. J. B. Hopkins, R. E. Gillilan, S. Skou, BioXTAS RAW: Improvements to a free open-source program for small-angle x-ray scattering data reduction and analysis. *J. Appl. Cryst.* **50**, 1545–1553 (2017).
77. K. Manalastas-Cantos, P. V. Konarev, N. R. Hajizadeh, A. G. Kikhney, M. V. Petoukhov, D. S. Molodenskiy, A. Panjkovich, H. D. T. Mertens, A. Gruzinov, C. Borges, C. M. Jeffries, D. I. Svergun, D. Franke, *ATSAS 3.0*: Expanded functionality and new tools for small-angle scattering data analysis. *J. Appl. Cryst.* **54**, 343–355 (2021).
78. D. I. Svergun, Determination of the regularization parameter in indirect-transform methods using perceptual criteria. *J. Appl. Cryst.* **25**, 495–503 (1992).
79. R. P. Rambo, J. A. Tainer, Accurate assessment of mass, models and resolution by small-angle scattering. *Nature* **496**, 477–481 (2013).
80. V. Piiadov, E. Ares de Araújo, M. Oliveira Neto, A. F. Craievich, I. Polikarpov, SAXSMoW 2.0: Online calculator of the molecular weight of proteins in dilute solution from experimental SAXS data measured on a relative scale. *Protein Sci.* **28**, 454–463 (2019).
81. D. Franke, C. M. Jeffries, D. I. Svergun, Machine learning methods for x-ray scattering data analysis from biomacromolecular solutions. *Biophys. J.* **114**, 2485–2492 (2018).
82. S. P. Meisburger, A. B. Taylor, C. A. Khan, S. Zhang, P. F. Fitzpatrick, N. Ando, Domain movements upon activation of phenylalanine hydroxylase characterized by crystallography and chromatography-coupled small-angle x-ray scattering. *J. Am. Chem. Soc.* **138**, 6506–6516 (2016).
83. S. Brenner, The genetics of *Caenorhabditis elegans*. *Genetics* **77**, 71–94 (1974).
84. G. A. Dokshin, K. S. Ghanta, K. M. Piscopo, C. C. Mello, Robust genome editing with short single-stranded and long, partially single-stranded DNA donors in *Caenorhabditis elegans*. *Genetics* **210**, 781–787 (2018).
85. J. Schindelin, I. Arganda-Carreras, E. Frise, V. Kaynig, M. Longair, T. Pietzsch, S. Preibisch, C. Rueden, S. Saalfeld, B. Schmid, J.-Y. Tinevez, D. J. White, V. Hartenstein, K. Eliceiri, P. Tomancak, A. Cardona, Fiji: An open-source platform for biological-image analysis. *Nat. Methods* **9**, 676–682 (2012).

Acknowledgments: We would like to thank A. Jaworski and M. E. Birnbaum for discussions and comments, H. Lee and the UIC Biophysics Core Facility for excellent service and support, S. Kordon and M. Zhao for help with electron microscopy data collection and processing, and M. Watkins and the Biophysics Collaborative Access Team (BioCAT) at the Argonne National Laboratory (ANL) for help with SAXS data collection and processing. **Funding:** This work was supported by the National Institutes of Health (NIH) grants R01 NS097161 to E.Ö., T32 GM138826 to J.M.P., and R35 GM147179 to J.L.M.; by the National Science Foundation Graduate Research Fellowship DGE-1656518 to E.L.N.; by the H2020 European Research Council fellowship MCSA-IF 702346 to R.G.S.; and by the Howard Hughes Medical Institute (HHMI), of which K.S. is an investigator. This research used resources of the Advanced Photon Source, a US Department of Energy (DOE) Office of Science User Facility operated for the DOE Office of Science by ANL under contract no. DE-AC02-06CH11357. Work at BioCAT was supported by grant P30 GM138395 from the National Institute of General Medical Sciences

(NIGMS) of the NIH. This study used resources of the GM/CA@APS, which is supported by the National Cancer Institute (ACB-12002) and the NIGMS (AGM-12006 and P30 GM138396). This work is also based on research conducted at the Northeastern Collaborative Access Team beamlines, which are funded by the NIGMS from the NIH (P30 GM124165). The Eiger 16M detector on the 24-ID-E beam line is funded by an NIH-ORIP HEI grant (S10OD021527). This study also used resources of the Berkeley Center for Structural Biology, supported in part by the HHMI, at the Advanced Light Source, a DOE Office of Science User Facility under contract no. DE-AC02-05CH11231. **Author contributions:** Conceptualization: E.Ö., K.S., R.M., J.L.M., J.M.P., and R.G.S. Methodology: J.M.P., E.L.N., R.G.S., J.B.H., J.L.M., R.M., K.S., and E.Ö. Validation: J.M.P., E.L.N., R.G.S., J.B.H., J.L.M., R.M., K.S., and E.Ö. Formal analysis: J.M.P., E.L.N., J.B.H., R.G.S., J.L.M., and R.M. Investigation: J.M.P., E.L.N., R.G.S., J.B.H., J.L.M., R.M., K.S., and E.Ö. Resources: E.Ö., K.S., R.M., and J.L.M. Data curation: J.M.P., E.L.N., R.M., and E.Ö. Writing—original draft: J.M.P., E.L.N., J.L.M., and E.Ö. Writing—review and editing: J.M.P., E.L.N., R.G.S., J.B.H., J.L.M., R.M., K.S., and E.Ö. Visualization: J.M.P., E.L.N., R.G.S., J.B.H., J.L.M., R.M., and E.Ö. Funding acquisition: E.Ö., K.S., R.M., J.L.M., and R.G.S. Supervision and project administration: E.Ö., K.S., R.M., and J.L.M. **Competing interests:** The authors declare that they have no competing interests. **Data and materials availability:** All data needed to evaluate the conclusions in the paper are present in the paper and/or the Supplementary Materials, except the following: The coordinates and crystallographic structure factors have been deposited in the PDB under the accession codes 8EDC (UNC-5 IG1 + 2) and 8EDI (UNC-5 IG1 + 2 with heparin-dp4), and 8EDK (UNC-6ΔC). SAXS datasets are deposited at the SASBDB under the accession codes SASDQJ9 (UNC-6ΔC–heparin–UNC-5 ECD) and SASDQK9 (UNC-6ΔC–heparin–UNC-5 ECD–UNC-40 ECD).

Submitted 20 July 2023
Accepted 17 January 2024
Published 16 February 2024
10.1126/sciadv.adj8083